

Joint synoptic and cloud variability over the Northeast Atlantic near the Azores

David B. Mechem¹, Carly S. Wittman¹
Matthew A. Miller², Sandra E. Yuter²,
and Simon P. de Szoeke³

¹Department of Geography and Atmospheric Science,
University of Kansas, Lawrence, Kansas

²Department of Marine, Earth, and Atmospheric Sciences
North Carolina State University, Raleigh, North Carolina

³College of Oceanic and Atmospheric Sciences
Oregon State University, Corvallis, Oregon *

July 26, 2017

**Corresponding author address:* David B. Mechem, Department of Geography and Atmospheric Science, University of Kansas, 1475 Jayhawk Blvd., 213 Lindley Hall, Lawrence, KS 66045-7613. E-mail: dmechem@ku.edu

Abstract

1
2 Marine boundary-layer clouds are modified by processes at different
3 spatial and temporal scales. In order to isolate the processes governing
4 aerosol–cloud–precipitation interactions, multi-day synoptic variability
5 of the environment must be accounted for. Information on the location of
6 low clouds relative to the ridge–trough pattern gives insight into how cloud
7 properties vary as a function of environmental subsidence, advection, and
8 stability. The technique of self-organizing maps (SOMs) is employed to
9 objectively classify the 500-mb geopotential height patterns for 33 years
10 of ERA–Interim reanalysis into pre-trough, trough, post-trough, ridge, and
11 zonal flow categories. The SOM technique is applied to a region of ma-
12 rine low clouds over the Eastern North Atlantic centered on the Azores
13 island chain, the location of a long-term Department of Energy observa-
14 tion site. The Azores consistently lie in an area of substantial variability in
15 synoptic configuration, thermodynamic environment, and cloud properties.
16 The SOM method was run in two ways to separately emphasize multi-
17 day and seasonal variability. Over and near the Azores, there is an east-
18 to-west sloshing back and forth of the western edge of marine low clouds
19 associated with different multi-day synoptic states. The different synop-
20 tic states also exhibit substantial north–south variability in the position of
21 high clouds. For any given month of the year, there is large year-to-year
22 variability in the occurrence of different synoptic states. Hence, estimating
23 cloud climatology from short-term field campaigns has large uncertainties.
24 This SOM approach is a robust method broadly applicable to characteriz-

ing synoptic regimes for any location.

26 **1. Introduction**

27 Observations of marine boundary layer (MBL) clouds show that they are highly
28 variable over a wide range of spatial and temporal scales (Klein et al. 1995;
29 Klein 1997; Caldwell et al. 2005; Stevens et al. 2005; Wood and Hartmann 2006;
30 Burleyson et al. 2013; de Szoeki et al. 2016). Untangling the relative sensitivity
31 of low cloud fraction to aerosol–cloud–precipitation interactions as a function of
32 synoptic-scale¹ ($L \sim 1000$ km) changes in the environment requires quantifica-
33 tion of the environmental context (e.g., Coopman et al. 2016). Information on
34 where the low clouds are located relative to the ridge–trough pattern gives in-
35 sight into how cloud properties vary as a function of environmental subsidence,
36 advection, and stability.

37 Low clouds are frequently found within synoptic waves at locations corre-
38 sponding to several distinct well-known associations between clouds and atmo-
39 spheric circulation patterns (Lau and Crane 1995, 1997). MBL stratocumulus
40 can exist under a number of different synoptic configurations. Stratocumulus
41 often occur east of the mid-tropospheric ridge axis, where the presence of a sub-
42 tropical high is associated with large-scale subsidence (Norris 1998; Norris and
43 Klein 2000). Stratocumulus are also frequently found behind the surface trough,
44 in the region of cold-air advection (Mechem et al. 2010). Stratocumulus and
45 optically thick stratus can also be present in the cyclone warm sector (Lau and

¹For the purposes of this paper, we use the terms synoptic-scale and large-scale synonymously, since baroclinic synoptic-scale waves are embedded in a slowly varying large-scale flow, and the synoptic-scale low pressure systems preferentially form in large-scale trough regions.

46 Crane 1997).

47 The Azores islands in the northeast Atlantic have served as a site for several
48 field campaigns to study low-cloud transitions. The Atlantic Stratocumulus Tran-
49 sition Experiment (ASTEX, Albrecht et al. 1995) in June 1992 used a combi-
50 nation of island, aircraft, ship, and satellite measurements to study the transition
51 from stratocumulus to trade cumulus. Substantial variations in cloud proper-
52 ties were found between clean marine and more polluted air masses of continen-
53 tal origin. In the summer, the environment near the Azores is dominated by the
54 subtropical Bermuda High (Hasanean 2004; Li et al. 2011). Additionally, weak
55 synoptic influence from cyclones to the north of the Azores affects the prevail-
56 ing wind direction and hence air-mass origin. The 18-month Clouds, Aerosol,
57 and Precipitation in the Marine Boundary Layer project (CAP-MBL, Wood
58 et al. 2015) centered on Graciosa Island (39.09°N, 28.03°W, 15.24 m altitude)
59 examined the interactions among clouds, aerosol, and precipitation through-
60 out the year. Rémillard et al. (2012) found that low clouds were the dominant
61 cloud type (present 40–60% of the time) year-round with the highest frequen-
62 cies of occurrence in summer and fall. Multi-year observations of clouds from
63 Graciosa Island are currently being made as part of the Department of Energy’s
64 Atmospheric Radiation Measurement Program Eastern North Atlantic (ENA)
65 fixed site ([https://www.arm.gov/capabilities/observatories/](https://www.arm.gov/capabilities/observatories/ena)
66 [ena](https://www.arm.gov/capabilities/observatories/ena)).

67 Accounting for environmental context helps to disentangle the roles of
68 physical mechanisms that may be simultaneously active in low-cloud systems.

69 For example, Myers and Norris (2013) used satellite data and reanalysis at sea-
70 sonal time scales to examine variations in cloud properties as a function of inver-
71 sion strength for the same value of subsidence, and variations in cloud properties
72 as a function of subsidence for the same value of inversion strength. Their results
73 yielded important new insights on climate sensitivity of low clouds to stronger
74 inversions and weaker subsidence. This paper follows the philosophy of My-
75 ers and Norris (2013) by setting the stage for examination of the most relevant
76 physical mechanisms underlying the observed *multi-day* variability of low-cloud
77 fields near the Azores. To this end, we characterize the synoptic state in an ob-
78 jective and unsupervised manner using the approach of self-organizing maps
79 (SOMs). The SOM method applied to the 500-mb geopotential height field from
80 reanalysis is combined with cloud information from satellite observations and
81 additional quantities from reanalysis to document the dominant synoptic states
82 and their characteristic cloud properties. We classify based on synoptic state and
83 then examine cloud properties associated with each synoptic state, since we are
84 interested in attributing behaviors of cloud properties to specific forcings. The
85 approach of classifying based on cloud properties and then examining the mete-
86 orological conditions (e.g., Rémillard and Tselioudis 2015) permits the possi-
87 bility that the same cloud type can occur in very different synoptic states, which
88 makes attribution to specific physical forcing mechanisms ambiguous. A broader
89 aim for our study is to advocate for the SOM approach as a robust and broadly
90 applicable method to characterize synoptic regimes for any given location.

91 **2. Methods and data**

92 *a. Approaches to synoptic classification*

93 A number of synoptic classification techniques exist, each with inherent assump-
94 tions and advantages, but all with the overarching goal of characterizing different
95 phases of the synoptic-scale wave pattern into classes, and the relation of atmo-
96 spheric properties to each class (Hewitson and Crane 2002). The concept of syn-
97 optic classification extends as far back as the late 19th century (Köppen 1874;
98 Abercromby 1883), and early synoptic classifications (also termed “synoptic typ-
99 ing”) were done manually (e.g., Lamb 1950). Though this method was effective,
100 it was labor intensive.

101 A number of automated approaches have been developed to alleviate the
102 labor-intensive nature of synoptic typing, chief among them linear decompo-
103 sition methods like empirical orthogonal functions (EOFs), k -means cluster-
104 ing, and self-organizing maps. The approach of SOMs is an automated neural
105 network (ANN) technique that produces a user-defined number of data states
106 (synoptic regimes, in our case), continuously distributed and spanning the data
107 parameter space (Hewitson and Crane 1992; Kohonen 2001). SOMs have been
108 employed for synoptic and climate classification (Cavazos 2000; Reusch et al.
109 2007; Bailey et al. 2011; Kennedy et al. 2016), cloud classification (Ambroise
110 et al. 2000), and extreme weather (Cassano et al. 2006). The SOM analysis pro-
111 duces a continuous distribution of synoptic regimes ranging from trough to ridge
112 (Hewitson and Crane 2002). Decomposing synoptic patterns into a continuum of

113 regimes using SOMs has an advantage over linear methods like EOF decompo-
114 sition, which produces orthogonal basis functions in space (EOFs) that may or
115 may not bear any resemblance to actual physical structures.

116 All synoptic classification approaches share a common goal of maximiz-
117 ing within-group similarity while minimizing between group similarity (Balling
118 1984). SOMs are similar to other traditional forms of cluster analysis, such as
119 *k*-means clustering, where nodes are distributed within a cloud of data, assigning
120 more nodes in regions of higher densities of data. The main difference between
121 SOMs and *k*-means clustering lies in the primary goal of the SOM, which is to
122 create a continuum of nodes that cumulatively represent the multi-dimensional
123 distribution of the entire data set, rather than simply representing individual
124 clusters of data. The SOM procedure is characterized by a competitive learn-
125 ing process that directs input data to its best matching (“winning”) node. As the
126 competitive learning process takes place, nodes surrounding the winning node
127 (“neighborhood” nodes) adjust toward the winner. This learning stage employs
128 a neighborhood function to update not only the winning node but also the sur-
129 rounding nodes as well. This neighborhood function is what distinguished SOMs
130 from a *k*-means clustering approach. The competitive learning and adjustment of
131 the nodes is self-defined based on the data alone and not dictated by preconcep-
132 tions of how the synoptic patterns should be distributed. Thus the SOM analysis
133 constitutes an unsupervised learning process, ultimately resulting in an objective
134 classification of synoptic states.

135 ***b. Data***

136 The SOM calculations are based on ERA–Interim (ERA–I) reanalysis (Dee
137 2011) from the CISL Research Data Archive (managed by NCEP with data from
138 ERA–I products, <http://rda.ucar.edu/>). The 6-hourly reanalysis prod-
139 ucts lie on a $0.7^\circ \times 0.7^\circ$ grid and span the period from January 1979 to Octo-
140 ber 2012. The analysis employs geopotential height and vertical velocity at the
141 1000-mb, 850-mb, 700-mb and 500-mb pressure levels, while cloud fraction
142 (CF), temperature, and cloud liquid- and ice-water mixing ratios (condensate)
143 are obtained for all available pressure levels.

144 Stability of the MBL inversion is quantified using estimated inversion strength
145 (EIS, Wood and Bretherton 2006):

$$EIS = (\theta_{700} - \theta_{surface}) - \Gamma_m^{850} (z_{700} - LCL), \quad (1)$$

146 where Γ_m^{850} is the moist adiabatic lapse rate at the 850-mb pressure level, LCL
147 is the height of the lifting condensation level, z_{700} is the height of the 700-mb
148 pressure level, and θ_{700} and $\theta_{surface}$ are the potential temperatures of the 700-mb
149 level and surface, respectively.

150 Projections of MODIS and ERA–I cloud fraction onto the SOM nodes illus-
151 trate the mean spatial distribution of cloud cover for each node. We also exam-
152 ine cloud-top temperature and total condensate as complementary measures of
153 cloud properties. Cloud fraction profiles from the reanalysis pressure levels are

154 employed to calculate total cloud fraction using the standard maximum-random
 155 overlap assumption (Morcrette and Fouquart 1986; Oreopoulos and Khairout-
 156 dinov 2003). This maximum-random overlap assumption assumes that adja-
 157 cent layers are overlapped maximally, while nonadjacent blocks are overlapped
 158 randomly. This relationship is given in (2) below, where C_1 represents the first
 159 cloud layer, and C_i and C_{i-1} represent adjacent cloud layers.

$$C_{maxran} = 1 - (1 - C_1) \times \prod_{i=2}^N \frac{1 - \max(C_{i-1}, C_i)}{1 - C_{i-1}} \quad (2)$$

160 Cloud top temperature (CTT) in the reanalysis is calculated using the high-
 161 est point at which cloud is present, using liquid- and ice-water content thresh-
 162 olds. Given the discrete nature of the pressure levels in the data set, the actual
 163 highest point of cloud may be underestimated somewhat, and therefore CTT
 164 may be overestimated (too warm). We found that the CTT calculation was not
 165 particularly sensitive to threshold values of liquid- or ice-water content. For the
 166 reanalysis vertical grid and a standard atmospheric lapse rate of 6.5 K km^{-1} , a
 167 1-gridpoint uncertainty in classifying cloud top yields CTT uncertainty estimates
 168 of at most 1.5 K at 900 mb and 4.8 K at 500 mb.

169 MODIS (Moderate Resolution Imaging Spectroradiometer) retrievals (Plat-
 170 nick et al. 2003) from the Aqua satellite (approximately 0130 and 1330 local
 171 time overpasses) supply the primary measures of cloud properties over the ENA.
 172 These data span the period from 2002 to 2012 and are used in conjunction with
 173 the reanalysis. Though nighttime Terra retrievals (10:30 pm) are closer in time

174 to the 0000 UTC ERA–I data used, nighttime Aqua retrievals (1:30 am) are used
175 because of a spurious, persistent, cone-shaped artifact in the Terra cloud frac-
176 tion products. MODIS cloud fraction properties come from the MYD08_L3 daily
177 global product available on a $1^\circ \times 1^\circ$ equal area grid ([https://modis-atmosphere.
178 gsfc.nasa.gov/MOD08_D3/index.html](https://modis-atmosphere.gsfc.nasa.gov/MOD08_D3/index.html)). Comparing MODIS cloud re-
179 trievals with cloud properties calculated from reanalysis is not trivial, largely
180 because of the possibility of overlapped clouds. The presence of high cloud will
181 mask low cloud and cause a systematic underestimate of low/liquid cloud frac-
182 tion. To sidestep this difficulty, we examine MODIS estimates of total cloud
183 fraction and cloud top temperature (which we take as a measure of the highest
184 layer) from the MYD08_L3 Cloud_Mask_5km MODIS product.

185 *c. Self-organizing maps*

186 Following the approach of Hewitson and Crane (2002), we employ the technique
187 of self-organizing maps to classify synoptic regime. Although some studies base
188 their synoptic regime classification on surface pressure or 1000-mb geopoten-
189 tial heights (Hewitson and Crane 2002), we select the 500-mb level because the
190 overwhelming dominance of the Bermuda High (particularly during the sum-
191 mer months) renders the 1000-mb height field a poor discriminator of synoptic
192 regime. Furthermore, the 500-mb level plays a central role in governing mid-
193 latitude dynamics.

194 The analysis domain is a grid of 42 points (latitude) by 57 points (longi-

195 tude), covering the outlined area in Fig. 1a lying between approximately 25° to
 196 55°N and 50° to 10°W. This area is roughly centered on Graciosa Island, site of
 197 the CAP–MBL field campaign (Wood et al. 2015). A number of sensitivity tests
 198 established this domain as roughly the best analysis domain area for our pur-
 199 poses. Smaller areas were not big enough to represent synoptic wave structure;
 200 larger areas tended to overly emphasize prominent climatological structures (par-
 201 ticularly the Icelandic Low), which then dominated the regime classification. We
 202 run the SOM algorithm on each month, and we chose to highlight January and
 203 June because of their significance to the annual cloud cycle.

204 When raw 500-mb heights were used in early tests of our SOM analysis,
 205 variability over northern latitudes exerted undue influence on the synoptic classi-
 206 fication. For this reason, we instead employ normalized anomalies of the 500-mb
 207 height field, calculated over the 33-year span of the reanalysis dataset:

$$\langle Z \rangle = \frac{Z - \bar{Z}}{\sigma_Z} \cos \phi, \quad (3)$$

208 where Z is the 500-mb geopotential height; \bar{Z} is a mean 500-mb height, calcu-
 209 lated over some time interval; σ_Z is the standard deviation calculated over that
 210 same interval; and ϕ is latitude. An equal area assumption is applied ($\cos \phi$) to
 211 avoid unduly weighting the polar regions (Gong and Wang 1999).

212 Anomalies are calculated using either monthly averaging windows, or a
 213 window the length of the entire reanalysis dataset available at the time. For the
 214 month-by-month classifications, the normalization is calculated by subtracting

215 a 31-day centered, running mean (± 15 days) from each data sample, and then
216 dividing that day by the standard deviation of that 31-day window. Calculating
217 anomalies based on monthly mean and standard deviation is in effect a high-
218 pass filter that removes variability at monthly periods and longer, leaving the
219 multi-day (synoptic) variability untouched. Running the SOM analysis on the
220 monthly-window anomalies emphasizes multi-day synoptic variability, which
221 can include, for example, intrusions of weak troughs into the Azores region dur-
222 ing the summer when the Bermuda High is dominant. Running the SOM anal-
223 ysis on anomalies based on a mean and standard deviation taken from the entire
224 length of the reanalysis, on the other hand, emphasizes the seasonal cycle.

225 The SOM is applied to the normalized anomalies for 500-mb geopotential
226 heights at 0000 UTC. We find that a once-daily snapshot of the synoptic state at
227 0000 UTC is sufficient for characterizing the synoptic classification. Further-
228 more, the classification is insensitive to the choice of specific time; the clas-
229 sification based on 1800 UTC reanalysis, for example, varies little from 0000
230 UTC. After the nodes are constructed, each 500-mb synoptic state is mapped to
231 a node that best resembles its configuration by minimizing a Euclidean distance
232 between the two. Each SOM node is therefore associated with a set of dates that
233 are uniquely mapped to that particular node.

234 *d. Choice of number of nodes*

235 The number of nodes is an important user-defined parameter. In order to repre-
236 sent the full continuum of synoptic behavior for over 30 years of data, it is im-
237 perative to choose a sufficient number of nodes. Too few nodes overgeneralize
238 the data and potentially combine distinct states into too few categories; too many
239 nodes, on the other hand, create an overwhelming number of synoptic states to
240 decipher, with similar synoptic states spread across multiple nodes. One way to
241 identify an optimal number of nodes is to run the SOM algorithm across a range
242 of different map sizes (from 2×2 to 10×10) and evaluate different SOM error
243 metrics.

244 We evaluated two error metrics across a number of map-size configurations,
245 and the number of nodes is determined by subjective competing constraints rep-
246 resented by these two error metrics. Following the concept of the elbow criterion
247 (Tibshirani et al. 2001), we calculate the quantization error (a measure of intran-
248 ode variability computed as the average Euclidean distance between the data and
249 its classified node) across the range of map sizes. The elbow criterion describes
250 the point at which the addition of nodes “fail to add a significant amount of in-
251 formation” (Schuenemann et al. 2009) to the SOM, justifying the lower bound
252 for number of nodes necessary to represent the input data. The topographic er-
253 ror (the proportion of all data samples for which the best-matched node and the
254 second-best-matched node are not adjacent in the node map, Kohonen 2001)
255 generally behaves in a manner opposite the quantization error, increasing with

256 the number of nodes as successive time levels of data become more likely to be
257 mapped to nonadjacent nodes. The point at which adding nodes drastically in-
258 creases the topographic error constitutes an upper bound for the ideal SOM size.
259 Our tests over this analysis region suggest that a map size of 25 nodes (5×5) is
260 optimal for this study.

261 *e. Projections of environmental and cloud properties*

262 At its core, the SOM analysis represents the mapping of each data point (specific
263 dates, in our case) to a node. Once the SOM procedure determines the nodes,
264 in principle any data source spanning the date range used to construct the nodes
265 can be composited (mapped) into node space. We refer to this process as “com-
266 positing” or “projecting” variables onto the nodes, acknowledging that this use
267 of the term projecting differs from standard EOF usage where data are projected
268 onto orthogonal basis structures. The projections of other atmospheric variables
269 from the reanalysis onto the SOM nodes more completely describes the synoptic
270 configuration.

271 We project a number of variables onto the SOM nodes, both from reanal-
272 ysis and from MODIS retrievals: 1000-mb geopotential heights, ERA-I and
273 MODIS total cloud fraction and cloud top temperature, total condensate (the
274 sum of liquid and ice water contents), stability measures, (estimated inversion
275 strength, EIS), and vertical velocity. It is important to note that these projected
276 variables have no influence on the actual SOM analysis itself (i.e., how the nodes

277 are determined), which employs only the normalized 500-mb geopotential height
278 anomaly field.

279 **3. Example of dominant synoptic configurations – June**

280 Figure 1 shows the mean 500-mb height structure for January and June. Our
281 analysis includes all months, but our discussion emphasizes June and January,
282 since those months exhibit maxima in total-cloud and low-cloud fraction (Rémillard
283 et al. 2012). The SOM nodes (numbered according to matrix notation) calcu-
284 lated for June are presented in Figure 2 as the positive (solid lines) and negative
285 (dashed lines) mean monthly-window anomalies for the data times mapped to
286 each specific node. Overlaid on the anomalies are the mean 500-mb geopoten-
287 tial heights projected on each node. The SOM node space spans continuum of
288 anomalies ranging from almost entirely positive values (node 35), half positive
289 and negative (nodes 53 and 13) and nearly all negative (node 31). The relative
290 frequency values for each node (Fig. 2) indicate that these archetypal nodes tend
291 to exhibit the highest frequencies among all the nodes. The middle node (33) is
292 characterized by a nearly uniform zero anomaly and may be interpreted as being
293 close to the climatological mean. Typically, successive 500-mb fields in time ex-
294 hibit a trajectory in node space around the edge states of the SOM, correspond-
295 ing to an evolution of the synoptic pattern (not shown).

296 Means of the 500-mb geopotential heights from the dates associated with
297 each node promote a meteorological interpretation of the SOM nodes. Positive

298 anomaly structures correspond to heights greater than climatology but not nec-
299 essarily a ridge-like structure. Note that the near-zero anomaly state (node 33)
300 corresponds to a structure slightly perturbed from simple zonal flow, with the
301 Azores lying just east of a weak ridge axis and just very west of a weak trough
302 axis. Nodes 35 and 31 are characterized by ridge and trough axes, respectively,
303 centered over the Azores. The Azores lie in a region of strong 500-mb geopo-
304 tential height gradients in two other very frequent nodes (53 and 13). We denote
305 these nodes as archtypal “pre-trough” (node 53) and “post-trough” (node 13)
306 patterns determined by the location of the trough axis relative to the Azores.
307 Though the geopotential heights over the analysis domain rarely drop below
308 5400-m in June, the Azores regularly experience the influence of synoptic ac-
309 tivity (e.g., nodes 41, 31, and 21). These nodes represent an intrusion of synoptic
310 low-pressure systems over the Azores.

311 Based on the position of the 500-mb ridge and trough axes relative to the
312 Azores, for each month we further cluster each node into different synoptic
313 categories. Although objective methods for classifying SOM nodes exist (e.g.,
314 Vesanto and Alhoniemi 2000), we classify the 25 nodes by hand based on the
315 500-mb geopotential heights and anomalies, using our understanding of the
316 structure of midlatitude synoptic systems. Additionally, some months contain
317 “unclassified” nodes. The most extreme or high frequency nodes are easiest to
318 classify. Nodes more difficult to classify, for example at the transition of dif-
319 ferent classes, typically have fewer data times mapped to them (i.e., lower fre-
320 quency) such that these difficult-to-classify nodes will little impact on the fre-

321 quency of the different classes. Supplemental figures S1–S12 show the SOM
322 nodes and synoptic category breakdown for all twelve months.

323 **4. Annual cycle in synoptic regimes**

324 We characterize the annual cycle of synoptic regimes by applying the SOM anal-
325 ysis to the monthly-window anomalies (calculated using the centered/running
326 mean and standard deviation) for each month calculated as described above, and
327 then classifying the nodes into pre-trough, trough, post-trough, ridge, or zonal
328 categories. This exercise results in the annual cycle presented in Table 1 and
329 shown in Fig. 3a, which indicates that all the different synoptic configurations
330 are present in each month. Particularly noteworthy is the result that June ex-
331 periences synoptic intrusions (trough regimes) 20.5% of the time, a frequency
332 greater than what might be expected given the dominant Bermuda High in the
333 summertime months. This breakdown using month-by-month classifications ac-
334 curately reflects the synoptic variability at any given time relative to what typi-
335 cally occurs in that month. We note, of course, that the trough classification in
336 January is substantially different (much stronger) than the June trough classifica-
337 tion.

338 Performing the SOM analysis using anomalies based on the mean and stan-
339 dard deviation from the entire dataset results in only a single classification (trough,
340 pre-trough, etc.) for the entire annual cycle. In this approach, the trough classi-
341 fication is characteristic of the strong troughs present during the winter, and the

342 ridge classification represents conditions of the summertime Bermuda High. For
343 this reason, summer is dominated by ridge and zonal patterns, whereas winter is
344 predominately trough and post-trough type patterns (Table 2 and Fig. 3b). This
345 annual perspective of the data set (Fig. 3b) does not exhibit the trough classifi-
346 cation during the summer months and therefore misses the synoptic intrusions
347 identified in the monthly analysis shown in Fig. 3a. Similarly, these anomalies
348 indicate that the winter months are dominated almost exclusively by trough and
349 post-trough weather patterns, without any ridge features. Fig. 3a shows, on the
350 other hand, that ridges are clearly present in the wintertime months.

351 The differences in these two approaches lie in how the classifications are
352 defined. Using only a single SOM node space for the entire year means that win-
353 ter months will tend to map to more trough-like nodes, and summer months will
354 map to more ridge-like nodes. Our analysis focuses on synoptic variability, and
355 therefore anomalies based on monthly-window means (e.g., Fig. 3a) will better
356 characterize how any given synoptic state compares to climatological behavior in
357 its given month.

358 Fig. 4 shows that January or June in any given year may not be representa-
359 tive of the long-term average distribution of synoptic behavior. This result sug-
360 gests that extreme caution should be used when interpreting the generality of
361 conclusions reached from short-term field deployments and encourages long-
362 term field data collection efforts.

363 **5. Dominant synoptic and cloud regimes — June**

364 *a. Synoptic properties*

365 In the previous section, we classify nodes together according to synoptic cate-
366 gory (trough, ridge, etc.) in order to calculate the frequency of each broad cate-
367 gory. However, compositing the synoptic and cloud structures themselves tends
368 to overgeneralize the states for the purpose of interpretation of the synoptic and
369 cloud structures. For this reason, we take the most-frequent nodes found on the
370 middle-edges of Fig. 2 as archetypes of the four synoptic patterns over the North
371 Atlantic region in June. Figure 5 shows these dominant synoptic states in terms
372 of the composited environmental variables. The pre-trough pattern shows that
373 the Azores lie in a tight gradient of 500-mb heights, with the trough axis near the
374 western portion of the domain. At 1000-mb, a weak Bermuda High is present
375 south and east of the Azores, and a low pressure center is present in the north-
376 west portion of the domain. This 1000-mb trough is roughly co-located with
377 the 500-mb trough axis. The Bermuda High is least dominant in this synoptic
378 state, reflected in its smallest spatial extent compared to the other archetypes and
379 the presence of the weak Icelandic Low, which is present only in this pattern.
380 The vertical motion field is consistent with the 500-mb geopotential height field,
381 specifically with upward vertical motion accompanying regions of positive dif-
382 ferential vorticity advection downstream of the trough axis.

383 EIS exhibits a tongue of low values oriented from southwest to northeast,
384 with smaller values equatorward and to the west. This tongue of low EIS val-

385 ues is present during June in all of the dominant states, and fine details in the
386 position and magnitude of this EIS tongue are consistent with the vertical mo-
387 tion field. Specifically, areas of strong subsidence at 500-mb are associated with
388 greater stability and a westward displacement of the low-EIS tongue. In the pre-
389 trough state, the Azores experience low values of EIS and lie on the border be-
390 tween upward and downward vertical motion at 500-mb, depending on the loca-
391 tion of the trough axis at 500-mb.

392 The trough pattern shows a weak positively tilted 500-mb trough located
393 over and to the southwest of the Azores. The 500-mb trough is evidently not
394 sufficiently strong to promote development of a surface low, but the pattern ex-
395 hibits a weaker low-level Bermuda High compared to the post-trough and ridge
396 regimes. The weak trough does not exhibit the robust region of ascent down-
397 stream of the trough axis as in the pre-trough pattern. Subsidence is widespread
398 in this state, which encourages greater stability values across the northern and
399 eastern portions of the domain (with the exception of the most northwestern por-
400 tion of the domain, which is strongly influenced by extremely cold waters that
401 enhances stability in the area). Over the Azores, both the trough and pre-trough
402 patterns exhibit similar EIS values.

403 The post-trough pattern shows the 500-mb trough axis on the far eastern
404 portion of the domain, with the Azores just east of a ridge axis. The Bermuda
405 High is strong at this state, and is co-located with the 500-mb ridge axis. The
406 tongue of low stability is restricted to the western-most portion of the domain.
407 The strongest subsidence is found in this synoptic state, with a maximum located

408 downstream of the 500-mb ridge axis. This strong subsidence promotes larger
409 EIS values over the Azores compared to the pre-trough and trough states, mak-
410 ing this the most stable synoptic state experienced by the Azores region. A small
411 region of low-EIS values is associated with the trough axis on the easternmost
412 region of the domain.

413 The ridge pattern exhibits the greatest 500-mb heights, with the ridge axis
414 centered over the Azores. The Bermuda High at 1000-mb is similar in structure
415 to that in the post-trough state, but the high-pressure system is more centered
416 over the Azores and does not extend as far north. Subsidence dominates much
417 of the southern portion of the domain, with a maximum downstream of the ridge
418 axis. The EIS structure in the ridge regime is similar to the post-trough state,
419 but the eastern portion of the domain is dominated by larger EIS values, likely
420 because of more widespread subsidence leading to stronger stability. The Azores
421 lie along a west-east gradient in stability, as they do in the post-trough state.

422 *b. Cloud properties*

423 Each of the four archtypal regimes in Fig. 6 exhibits a shield of cold clouds to
424 the northwest, as well as warm, low stratocumulus clouds to the southeast. Fig-
425 ure 6 also indicates that the ERA-I cloud fraction is systematically smaller than
426 cloud fraction estimates from MODIS, but patterns of cloud fraction and CTT
427 are often in reasonable agreement. We chose to show the mean, but in principle
428 any measure of central tendency could be used, as well as measures of variance

429 or even the full probability distribution function (PDF).

430 In the pre-trough state, the Azores lie within a strong gradient (NW–SE) in
431 condensate and cloud fraction, with both quantities increasing toward the north-
432 west. These cloud structures lie downstream of the trough axis in Fig. 5 and ap-
433 pear to be associated with areas of strong upward vertical motion from Figure
434 5. On average, these are mixed-phase clouds ($CTT < 250$ K). Condensate and
435 cloud fraction decrease substantially toward the south and southeast, except for a
436 small tongue of larger cloud fraction east and southeast of the Azores. This area
437 of warm, low cloud (stratocumulus, most likely) is evident in both the MODIS
438 data and reanalysis. These low clouds lie in an area of subsidence and modestly
439 stable values of EIS ($\sim 4\text{--}5$ K). In this regime, the Azores lie near the strongest
440 part of the gradient in cloud fraction and CTT, and therefore may experience ei-
441 ther low-altitude liquid stratocumulus or higher-altitude frontal clouds associated
442 with synoptic systems influencing the region.

443 The trough pattern shows colder cloud tops displaced toward the south and
444 southeast portions of the domain. In this regime, the Azores lie well inside the
445 synoptic cloud shield. The steepest gradient in ERA–I condensate, cloud frac-
446 tion, and CTT is less evident in the MODIS cloud fields, which display a less
447 coherent signal. In fact, the MODIS retrievals exhibit a substantial northward
448 intrusion of warm cloud tops (low clouds) that in the reanalysis is present only
449 over the easternmost portion of the domain.

450 In the post-trough state, total condensate is more extensive over the southern
451 portion of the domain than in pre-trough and trough states. The area of strong

452 subsidence in Figure 5 and low CTTs for this pattern indicates that the majority
453 of the clouds over and to the east, south and southwest of the Azores are stra-
454 tocumulus clouds. The spatial configuration of ERA-I and MODIS cloud frac-
455 tions are quite similar in this regime. These stratocumulus are found downstream
456 of the 500-mb ridge axis and over the eastern portion of the Bermuda High, in
457 a region of stronger EIS values. The areas of maximum total condensate, and
458 ERA-I and MODIS cloud fraction are collocated with areas of ascent in the
459 northwestern portion of the domain and do not reach as far south as in the pre-
460 trough state. The warm cloud tops indicate that stratocumulus are the dominant
461 cloud type over the Azores in the post-trough state.

462 Because of the strong gradient in vertical motion and strong subsidence
463 downstream of the 500-mb ridge axis (Fig. 5), the ridge pattern most clearly il-
464 lustrates the different cloud regimes in the region. The area of ascent at 500-mb
465 in the far northwest is associated with condensate values as high as 200 g m^{-2} .
466 The clouds associated with this total condensate are cold ($\sim 260 \text{ K}$ for both MODIS
467 and reanalysis) and spatially extensive, with their boundary in the vicinity of the
468 Azores. North of the Azores, the cloud field transitions to warmer (i.e., lower)
469 cloud. This stratocumulus deck is encouraged by the subsidence maximum in
470 this state and lies in an area of stronger stability. Stratocumulus is most extensive
471 in this ridge pattern, which may be attributed to such high values of subsidence
472 downstream of the ridge axis. In this regime, cloud conditions at the Azores are
473 influenced by the southeastern stratocumulus deck and the relatively clear slot to
474 the southwest, which may modulate the Azores cloud field. The overlapping of

475 the regimes suggests an environment conducive to substantial variability in cloud
476 properties at the Azores.

477 In summary, these June cloud regimes suggest substantial variability in
478 cloud properties over the Azores. The Azores are located in a prime location
479 to experience both stratocumulus clouds and clouds associated with synoptic low
480 pressure systems. The position of the 500-mb wave and its associated vertical
481 motion field influence the cloud properties over the region.

482 **6. Dominant synoptic and cloud regimes — January**

483 *a. Synoptic properties*

484 The four synoptic configurations in Fig. 7 differ substantially from the June pat-
485 terns. In the pre-trough regime, the Azores lie in a region of weak ascent and
486 relatively low stability. The pre-trough pattern for January has strong north-south
487 gradients in 500-mb geopotential heights, indicative of a jet-like structure with a
488 maximum in the vicinity of the Azores. The trough axis is difficult to discern but
489 lies west of the Azores. The 1000-mb structure resembles a confluent trough and
490 also exhibits a strong north-south gradient. Given the jet structure at 500-mb, the
491 southwest and northeast regions of the domain constitute the right entrance and
492 left exit regions, an interpretation consistent with regions of ascent in the 500-
493 mb vertical velocity field. Broadly speaking, the magnitude of vertical velocity
494 in January is much greater than in June. Regions of ascent are associated with
495 smaller EIS values; stronger subsidence coincides with greater stability. The far

496 northwest region of the domain is the most stable, and this feature is present in
497 all of the synoptic patterns (and in June as well) because of the cold surface tem-
498 peratures in this area. The baseline “tongue” of low EIS values seen consistently
499 in June (Fig. 5) is not present in January, when EIS varies much more across the
500 different synoptic regimes.

501 The trough regime has an easily distinguishable trough axis lying just west
502 of the Azores. At 1000-mb, the Icelandic Low is so dominant that the Bermuda
503 High is not present. The Icelandic (surface) Low is centered northwest of the is-
504 lands, with its trough axis just downstream of the upper level trough axis. Most
505 of the center portion of the domain, including the Azores region, is dominated by
506 strong ascent, although subsidence is present on the western and north-northeastern
507 regions of the domain. This strongest ascent in the center of the domain corre-
508 sponds to a bullseye of the lowest EIS values.

509 The post-trough regime is characterized by a positively tilted ridge/trough
510 pair. The 500-mb ridge axis is oriented from the southwest to the northeast over
511 the western part of the domain, and the trough axis is located across the south-
512 east corner of the domain. This positively-tilted ridge encourages the presence
513 of an elongated Bermuda High, with its maximum directly north of the Azores.
514 Strong subsidence is present over and downstream of the ridge axis (both 500
515 and 1000 mb), across a region characterized by high values of 1000-mb geopo-
516 tential height. Enhanced stability accompanies much of this large region of sub-
517 sidence, with the Azores lying near a strong gradient in EIS. Weak stability is
518 found downstream of the trough axis in a region of ascent next to the African

519 coastline.

520 A positively tilted 500-mb ridge lying over the Azores characterizes the
521 ridge regime. Large values of 1000-mb geopotential height show the presence of
522 a strong Bermuda high, centered just east of the Azores, that dominates much of
523 the analysis domain. A dipole of vertical velocity straddles the ridge, with sub-
524 sidence present over the eastern half of the high and ascent west of the 500-mb
525 ridge axis. The influence of the vertical velocity couplet is evident in the intru-
526 sion of low EIS to the west of the Azores, and a region of high stability to the
527 east. Large values of EIS are found in the northern and eastern portions of the
528 domain, the latter region being where stratocumulus decks tend to persist in the
529 summertime months. In the January ridge regime, however, subsidence and sta-
530 bility are even stronger and more spatially widespread than in June.

531 The month of January shows much more variability across the different syn-
532 optic regimes than does June. Regions of substantial large-scale ascent associ-
533 ated with midlatitude synoptic systems reach lower latitudes in winter, allowing
534 these latitudes to experience sustained periods of ascent. January exhibits both
535 stronger ascent and descent compared to June, and the Azores lie long the tran-
536 sition between ascent and descent (pre-trough and ridge regimes). The Icelandic
537 Low exerts a strong influence during wintertime months, which seems to be the
538 ultimate source of much of the meteorological variability across the patterns,
539 as the low develops and modulates the strength and persistence of the Bermuda
540 High.

541 ***b. Cloud properties***

542 Mean January cloud properties associated with each characteristic synoptic
543 regime (Fig. 8) show that the synoptic and cloud structures exhibit more varia-
544 tion across the pattern than the characteristic patterns for Jun (cf. Fig. 6). In the
545 pre-trough state, large values of cloud fraction are present over the majority of
546 the domain in both the reanalysis and MODIS, except for the most southeast and
547 southwest regions. The total condensate field shows a strong gradient across the
548 Azores, and a local maximum in total condensate in the northeast portion of the
549 domain associated with the strong ascent from the left exit region of the jet-like
550 structure in this synoptic pattern (Figure 7). ERA-I and MODIS show similar
551 structures across the domain, but as previously seen, MODIS cloud fractions are
552 greater than those from reanalysis. Large values of cloud fraction prevail across
553 most of the domain, but differences in cloud-top temperature between MODIS
554 and reanalysis suggest differences in cloud type and behavior in the two datasets.
555 The coldest clouds in the reanalysis CTT lie in the area of ascent and are lo-
556 cated in the northern portions of the domain, extending southward to the Azores.
557 In the middle of the most southern portion of the domain, however, clouds are
558 present in both the total condensate and total cloud fraction for reanalysis and
559 MODIS. These clouds must be stratocumulus because of their warm CTT values
560 (around 280K), higher CF (close to 1.0 from MODIS), and lower total conden-
561 sate values (around 60 g m^{-3}).

562 The spatial structure of the reanalysis condensate in the trough regime is

563 oriented in a north-south configuration, with a maximum located just east of the
564 trough axis in Figure 7. These large values of condensate are also associated
565 with the location of strong ascent and weak stability. The CTT field from both
566 reanalysis and MODIS identifies these as cold clouds. This band of cold cloud
567 tops, however, is narrower in MODIS than in the reanalysis, and the MODIS
568 cloud band is more distinguishable in the CTT field than in the cloud fraction.
569 The cloud property structures (particularly total condensate and MODIS CTT)
570 are strikingly similar to the vertical velocity field.

571 In the post-trough state, clouds in the northwestern part of the domain are
572 strongly tied to the region of ascent upstream of the ridge axis (Fig. 7). Across
573 the southeast, both reanalysis and MODIS show a pocket of cold clouds in a re-
574 gion of ascent downstream of the trough axis. The area between the northwest-
575 ern cloud regime and the southeast cold pocket is comprised of warmer clouds in
576 a region of subsidence, suggesting stratocumulus. These clouds lie in a strong
577 gradient from weaker to stronger EIS, an unusual feature compared to other
578 regimes where stratocumulus is associated with broad regions of strong stability.
579 These clouds appear to be largely consistent with the post-cold-frontal stratocu-
580 mulus seen in Mechem et al. (2010).

581 As in June, the January ridge state exhibits two well-defined cloud regimes
582 as evident in the reanalysis total condensate and reanalysis and MODIS cloud-
583 top temperature. These cloud regimes represent mixed-phase clouds toward the
584 north, and the eastern ocean basin clouds. The distinct couplet of these cloud
585 types is associated with the vertical velocity and stability couplets from Figure

586 7. The northwest region, which is dominated by ascent, exhibits widespread cold
587 clouds and total condensate values of 200 g m^{-2} . Cold cloud-top temperatures
588 of $\sim 260 \text{ K}$ extend to the Azores. In the subsidence region associated with higher
589 stability downstream of the ridge axis in Figure 7, warmer cloud top tempera-
590 tures and lower total condensate values persist, suggesting stratocumulus. The
591 location and spatial coverage of these stratocumulus are similar to the stratocu-
592 mulus location and coverage in the June ridge regime.

593 One common theme of these analyses is that the Azores in January, as in
594 June, lie in a region of overlapping cloud types. The January synoptic regimes is
595 one of prevalent cloudiness, although details of cloud structure differ. Compared
596 to June, January exhibits far greater variability in both magnitude and spatial
597 distribution. In January, the Icelandic Low is predominantly responsible for the
598 modulation of the Bermuda High, and stratocumulus are associated with loca-
599 tions of 500-mb subsidence.

600 **7. Discussion and Conclusions**

601 de Szoeki et al. (2016) showed larger or similar variance in marine low cloud
602 cover associated with multi-day synoptic variability as compared to seasonal
603 variability in subtropical marine stratocumulus regions. Characterizing synop-
604 tic context is vital in developing insight into how MBL cloud properties respond
605 to synoptic-scale forcing mechanisms on multi-day timescales. Constraining
606 synoptic conditions is also a prerequisite to untangling internal cloud-system

607 aerosol–cloud–precipitation interactions. We chose to base our classification
608 on synoptic states and then composite cloud properties on those synoptic states,
609 the justification being that cloud properties are to first order an outcome of the
610 synoptic-scale environment and forcing. The alternate approach, a clustering
611 based on cloud properties (e.g., Rémillard and Tselioudis 2015), raises the pos-
612 sibility that similar clouds can occur under different synoptic states, making
613 a clear attribution to specific forcing mechanisms a challenge. An example of
614 clouds with similar physical characteristics originating under different conditions
615 are low marine clouds in regions with strong subsidence versus those in cold-air
616 outbreaks.

617 We employ the technique of self-organizing maps (SOMs) to develop a cli-
618 matology of synoptic and cloud patterns centered on the Azores islands in the
619 Eastern North Atlantic. The SOM approach, based on classifying normalized
620 500-mb geopotential height anomalies, is successful in identifying dominant
621 synoptic states. Compositing meteorological and cloud properties by synoptic
622 pattern provides insights into how clouds and their environment jointly vary
623 by synoptic state. The SOM approach identifies well-established patterns con-
624 sistent with long-standing understanding of the structure of mid-latitude baro-
625 clinic synoptic waves, and does so in an objective manner that can be applied to
626 large datasets. Unlike linear techniques such as PCA/EOF approaches, the SOM
627 method preserves the continuity across the different synoptic states.

628 Our discussion focuses on June and January because of their significance
629 in the annual cloud cycle. The Azores island chain ($\sim 39^\circ\text{N}$) consistently lies

630 in an area of substantial variability in both synoptic configuration and environ-
631 mental and cloud properties in comparison to the persistent MBL stratocumulus
632 regimes in the NE Pacific, SE Pacific, and SE Atlantic (25°N, 18°S, and 15°S,
633 respectively, Fig. 4 in Wood (2012)). The Azores has long been considered a
634 “transition” region in terms of cloud-regime transitions accompanying SST gra-
635 dients (Albrecht et al. 1995). It is *also* a transition region between the influences
636 of the semi-permanent subtropical highs and middle latitude synoptic waves.
637 The synoptic-scale variability has been largely underappreciated even though it
638 also modulates large-scale vertical motions and cloudiness. There are frequently
639 occurring high and middle clouds throughout the year (e.g., the daylight high-
640 cloud amount over the Azores of ~ 0.3 in Fig. 1a of de Szoeki et al. 2016) so
641 the radiative effects of low clouds without high clouds above them occur for
642 only a fraction of the domain and a portion of the time. Variability on synoptic
643 timescales is most evident when the SOM classification is performed on anoma-
644 lies calculated using monthly-window means and standard deviations, which act
645 as a high-pass filter that removes multi-month (seasonal) variability and longer.
646 Ridges, troughs, and transitional patterns are present for both January and July,
647 but these patterns must be understood in the context of both the monthly and an-
648 nual climatology in order to be interpreted correctly. A trough in January, for ex-
649 ample, is more intense (lower heights and stronger height gradient) than a trough
650 in June. The Azores exhibits a combination of the northern, cold, thick cloud
651 regime as well as the low cloud tops of stratocumulus. The highly variable na-
652 ture of the clouds at the Azores can be partially attributed to overlapping cloud

653 regimes.

654 June is dominated by the Bermuda High, and patterns with a weaker Bermuda
655 High permit synoptic intrusions into lower latitudes. There is an advance and
656 retreat of high-level clouds coming from the north, as well as a sloshing back
657 and forth of eastward-westward shifts of the stratocumulus deck along a roughly
658 WSW–ENE diagonal over the Azores (Fig. 6). When the upper-level ridge axis
659 is centered over the Azores, associated subsidence conditions east and southeast
660 of the Azores create ideal conditions for stratocumulus persistence. The base-
661 line “tongue” structure of EIS is modulated by sustained vertical velocity fields,
662 with subsidence associated with increased stability. Stratocumulus are dominant
663 downstream of this ridge axis, in regions of high stability. The summer months
664 have the highest amounts of low-level clouds at the Azores. Based on anomalies
665 calculated relative to the entire data set (Table 2), during June the relative fre-
666 quencies of different synoptic patterns in order of frequency of occurrence are
667 pre-trough (40%), ridge (34%), zonal flow (16%), post-trough (5%), unclassified
668 (4%), and trough (<1%). When the seasonal variability is removed by running
669 the SOM analysis on the running-monthly anomalies, the frequency of occur-
670 rence of the different synoptic patterns in June is more evenly distributed among
671 the nodes with 25% post-trough, 23% pre-trough, 22% ridge, 20% trough, and
672 10% zonal flow (Table 1).

673 January exhibits greater spatial variability in synoptic and cloud properties
674 and larger magnitude differences among synoptic patterns than in June. Instead
675 of the Bermuda High dominating synoptic properties, the Icelandic low modu-

676 lates most aspects of the synoptic regimes over the region. While the low pressure
677 centers associated with winter extratropical cyclones in the northeast Atlantic are
678 usually well north of the Azores, the southern portions of cold fronts can drape
679 over the islands. Again there is a sloshing back and forth both in the advance and
680 retreat of high-level clouds coming from the north which penetrate further south
681 than in June (Fig. 8). Low clouds occur to the SE of the Azores with the cloud
682 deck western edge forming a SW-NE diagonal that bisects the island chain dur-
683 ing monthly anomaly ridge conditions (Fig. 8). Based on anomalies calculated
684 relative to the entire data set (Table 2), during January the relative frequencies of
685 different synoptic patterns in order of frequency of occurrence are trough (37%),
686 post-trough (34%), unclassified (15%), pre-trough (12%), ridge (1%) and zonal
687 flow (<1%). When the seasonal variability is removed by running SOM on the
688 running-monthly anomalies, the frequency of occurrence of the different syn-
689 optic patterns in January is 25% ridge, 21% pre-trough, 17% trough, 17% zonal
690 flow, 10% unclassified, and 8% post-trough (Table 1). In winter, stratocumu-
691 lus near the Azores primarily occurs as post-cold-frontal stratocumulus with the
692 post-trough regime (Mechem et al. 2010).

693 The SOM approach outlined here is a general, robust, and broadly applica-
694 ble method of characterizing synoptic regimes for any given region. Depending
695 on the application, anomalies calculated relative to multiyear annual means, rela-
696 tive to running monthly means or both may be appropriate. These classifications
697 can place case studies into context of their synoptic environment as well as of the
698 multi-decade sample. For longer-term datasets, this method can identify dates

699 or periods with certain synoptic characteristics for focussed study. Lastly, our
700 results show that relative occurrence of synoptic patterns in any single year or
701 any given month at the Azores are unlikely to be representative of the climato-
702 logical behavior, suggesting caution when inferring long-term conditions from
703 short-term field campaigns.

704 *Acknowledgements*

705 The authors greatly appreciate advice and feedback from Adriana Bailey, Aaron
706 Kennedy, and Shu Chen. Many thanks to Maike Ahlgrimm for her tireless pa-
707 tience in answering our many questions about ERA–Interim details. Thanks
708 to Lucas McMichael for comments on the manuscript. All our SOM analyses
709 used the MATLAB SOM toolbox (<http://www.cis.hut.fi/projects/somtoolbox>).
710 This work was funded by Department of Energy Atmospheric Systems Research
711 grants DE–SC0006736 (Mechem), DE–SC0016522 (Mechem), DE–SC0006701
712 (Yuter), and DE–SC0006994 (de Szoeke). Mechem also acknowledges support
713 by the Office of Naval Research award N00014–11–1–0518.

714 **References**

- 715 Abercromby, R., 1883: On certain types of British weather. *Q. J. R. Meteorol.*
716 *Soc.*, **9**, 1–25.
- 717 Albrecht, B. A., C. S. Bretherton, D. Johnson, W. H. Schubert, and A. S. Frisch,

- 718 1995: The atlantic stratocumulus experiment — ASTEX. *Bull. Amer. Meteor.*
719 *Soc.*, **76**, 889–904.
- 720 Ambrose, C., F. Badran, and S. Thiria, 2000: Hierarchical clustering of self-
721 organizing maps for cloud classification. *Neurocomputing*, **30**, 47–52.
- 722 Bailey, A., T. N. Chase, J. J. Cassano, and D. Noone, 2011: Changing temper-
723 ature inversion characteristic in the u.s. southwest and relationships to large-
724 scale atmospheric circulation. *J. Appl. Meteor. Climatol.*, **50**, 1307–1323.
- 725 Balling, R. C., 1984: Classification in climatology. *Spatial statistics and models*,
726 81–108.
- 727 Burleyson, C. D., S. P. de Szoeke, S. E. Yuter, M. Wilbanks, and W. A. Brewer,
728 2013: Ship-based observations of the diurnal cycle of southeast pacific marine
729 stratocumulus clouds and precipitation. *Journal of the Atmospheric Sciences*,
730 **70**, 3876–3894.
- 731 Caldwell, P., C. S. Bretherton, and R. Wood, 2005: Mixed-layer budget analy-
732 sis of the diurnal cycle of entrainment in southeast Pacific stratocumulus. *J.*
733 *Atmos. Sci.*, **62**, 3775–3791.
- 734 Cassano, E. N., A. H. Lynch, J. J. Cassano, and M. R. Koslow, 2006: Classifica-
735 tion of synoptic patterns in the western Arctic associated with extreme events
736 at Barrow, Alaska, USA. *Clim. Res.*, **30**, 83–97.
- 737 Cavazos, T., 2000: Using self-organizing maps to investigate extreme climate

738 events: An application to wintertime precipitation in the Balkins. *J. Clim.*, **13**,
739 1718–1732.

740 Coopman, Q., T. J. Garrett, J. Riedi, S. Eckhardt, and A. Stohl, 2016: Effects
741 of long-range aerosol transport on the microphysical properties of low-level
742 liquid clouds in the arctic. *Atmospheric Chemistry and Physics*, **16**, 4661–
743 4674, doi:10.5194/acp-16-4661-2016.

744 URL <http://www.atmos-chem-phys.net/16/4661/2016/>

745 de Szoeke, S. P., K. L. Verlinden, S. E. Yuter, and D. B. Mechem, 2016: The
746 time scales of variability of marine low clouds. *J. Climate*, in press.

747 Dee, D. P. w. . c.-a., 2011: The era-Interim reanalysis: configuration and perfor-
748 mance of the data assimilation system. *Quart. J. R. Meteorol. Soc.*, **137**, 553–
749 597.

750 Gong, D. and S. Wang, 1999: Definition of antarctic oscillation index. *Geo. Res.*
751 *Lett.*, **26**, 459–462.

752 Hasanean, H., 2004: Variability of the north atlantic subtropical high and associ-
753 ations with tropical sea-surface temperature. *International journal of climatol-*
754 *ogy*, **24**, 945–957.

755 Hewitson, B. D. and R. G. Crane, 1992: Regional-scale climate prediction from
756 the giss gcm. *Global Planetary Change*, **97**, 249–267.

757 — 2002: Self-organizing maps: applications to synoptic climatology. *Clim. Res.*,
758 **22**, 13–26.

759 Kennedy, A. D., X. Dong, and B. Xi, 2016: Cloud fraction at the arm sgp site:
760 reducing uncertainty with self-organizing maps. *Theoretical and Applied Cli-*
761 *matology*, **124**, 43–54.

762 Klein, S. A., 1997: Synoptic variability of low-cloud properties and meteorolog-
763 ical parameters in the subtropical trade wind boundary layer. *J. Climate*, **10**,
764 2018–2039.

765 Klein, S. A., D. L. Hartmann, and J. R. Norris, 1995: On the relationships
766 among low-cloud structure, sea surface temperature, and atmospheric circu-
767 lation in the summertime northeast pacific. *J. Climate*, **8**, 1140–1155.

768 Kohonen, T., 2001: *Self-Organizing Maps, 3rd ed.*, volume 30. Springer Ser. Inf.
769 Sci., 501 pp.

770 Köppen, W., 1874: *Über die Abhängigkeit des klimatischen Charakters der*
771 *Winde von ihrem Ursprunge*. Methuen & Co Ltd., London, cited from ?.

772 Lamb, H. H., 1950: Types and spells of weather around the year in the british
773 isles: annual trends, seasonal structure of the year, singularities. *Q. J. R. Mete-*
774 *orol. Soc.*, **76**, 393–429.

775 Lau, N.-C. and M. W. Crane, 1995: A satellite view of the synoptic-scale orga-
776 nization of cloud properties in midlatitude and tropical circulation systems.
777 *Monthly weather review*, **123**, 1984–2006.

778 — 1997: Comparing satellite and surface observations of cloud patterns in
779 synoptic-scale circulation systems. *Monthly weather review*, **125**, 3172–3189.

780 Li, W., L. Li, R. Fu, Y. Deng, and H. Wang, 2011: Changes to the North Atlantic
781 subtropical high and its role in the intensification of summer rainfall variabil-
782 ity in the Southeastern United States. *J. Climate*, **24**, 1499–1506.

783 Mechem, D. B., Y. L. Kogan, and D. M. Schultz, 2010: Large eddy observations
784 of post-cold-frontal continental stratus. *J. Atmos. Sci.*, **67**, 3368–3383.

785 Morcrette, J. J. and Y. Fouquart, 1986: The overlapping of cloud layers in short-
786 wave radiation parameterizations. *J. Atmos. Sci.*, **43**, 321–328.

787 Myers, T. A. and J. R. Norris, 2013: Observational evidence that enhanced sub-
788 sidence reduces subtropical marine boundary layer cloudiness. *Journal of Cli-
789 mate*, **26**, 7507–7524.

790 Norris, J. R., 1998: Low cloud type over the ocean from surface observations.
791 part i: Relationship to surface meteorology and the vertical distribution of
792 temperature and moisture. *J. Climate*, **11**, 369–382.

793 Norris, J. R. and S. A. Klein, 2000: Low cloud type over the ocean from surface
794 observations. part iii: Relationship to vertical motion and the regional synoptic
795 environment. *J. Climate*, **13**, 245–256.

796 Oreopoulos, L. and M. Khairoutdinov, 2003: Overlap properties of clouds gener-
797 ated by a cloud-resolving model. *J. Geo. Res.*, **108**, 4479–4488.

798 Platnick, S., M. D. King, S. A. Ackerman, W. P. Menzel, B. A. Baum, J. C. Ridi,
799 and R. A. Frey, 2003: The modis cloud products: Algorithms and examples

800 from terra. *IEEE Transactions on geoscience and Remote Sensing*, **41**, 459–
801 473.

802 Rémillard, J., P. Kollias, E. Luke, and R. Wood, 2012: Marine boundary layer
803 cloud observations in the Azores. *J. Climate*, **25**, 7381–7398.

804 Rémillard, J. and G. Tselioudis, 2015: Cloud regime variability over the azores
805 and its application to climate model evaluation. *Journal of Climate*, **28**, 9707–
806 9720.

807 Reusch, D. B., R. B. Alley, and B. C. Hewitson, 2007: North atlantic climate
808 variability from a self-organizing map perspective. *Journal of Geophysical*
809 *Research: Atmospheres*, **112**, doi:10.1029/2006JD007460, d02104.
810 URL <http://dx.doi.org/10.1029/2006JD007460>

811 Schuenemann, K. C., J. J. Cassano, and J. Finnis, 2009: Synoptic forcing of pre-
812 cipitation over Greenland: Climatology for 1961-99. *J. Hydrometeor*, **10**, 60–
813 78.

814 Stevens, B., G. Vali, K. Comstock, M. C. van Zanten, P. H. Austin, C. S. Brether-
815 ton, and D. H. Lenschow, 2005: Pockets of open cells (POCs) and drizzle in
816 marine stratocumulus. *Bull. Amer. Meteor. Soc.*, **86**, 51–57.

817 Tibshirani, G., G. Walther, and T. Hastie, 2001: Estimating the number of clus-
818 ters in a data set via the gap statistic. *J. R. Statist. Soc.*, **63**, 411–423.

819 Vesanto, J. and E. Alhoniemi, 2000: Clustering of the self-organizing map. *Neu-
820 ral Networks, IEEE Transactions on*, **11**, 586–600.

- 821 Wood, R., 2012: Stratocumulus clouds. *Mon. Wea. Rev.*, **140**, 2373–2423.
- 822 Wood, R. and C. S. Bretherton, 2006: On the relationship between stratiform low
823 cloud cover and lower-tropospheric stability. *J. Climate*, **19**, 6425–6432.
- 824 Wood, R. and D. L. Hartmann, 2006: Spatial variability of liquid water path in
825 marine low cloud: The importance of mesoscale cellular convection. *Journal*
826 *of climate*, **19**, 1748–1764.
- 827 Wood, R., M. Wyant, C. S. Bretherton, J. Rémillard, P. Kollias, J. Fletcher,
828 J. Stemmler, S. deSzoeko, S. Yuter, M. Miller, D. Mechem, G. Tselioudis,
829 C. Chiu, J. Mann, E. O’Connor, R. Hogan, M. M. X. Dong, V. Ghate, A. Jef-
830 ferson, Q. Min, P. Minnis, R. Palinkonda, B. Albrecht, E. Luke, C. Hannay, ,
831 and Y. Lin, 2015: Clouds, Aerosol, and Precipitation, in the Marine Bound-
832 ary Layer: An ARM Mobile Facility Deployment. *Bull. Amer. Meteor. Soc.*,
833 **96**, 419–440.

834 **List of Figures**

835 1 Mean 500-mb heights for January and June. The inner box in the
836 top map represents the smaller domain used to explore variabil-
837 ity in the vicinity of the Azores. Black contour lines are standard
838 deviation of the mean 500-mb height, and can be used as a proxy
839 for storm track variability, where higher numbers indicate higher
840 variability. 44

841 2 Monthly-window SOM nodes of 500-mb geopotential heights
842 with overlaid contours of normalized 500-mb geopotential height
843 anomalies (using mean and standard deviation values calculated
844 over a 31-day window centered on each day) for June. The con-
845 tour interval for the height anomalies is 0.1 [nondimensional].
846 The numbers in the upper left-hand portion of each node indicate
847 node number in matrix notation, and the relative frequency of
848 occurrence of each node. 45

849 3 Annual cycle of ridge, zonal, pre-trough, trough, post-trough,
850 and unclassified patterns based on the anomalies calculated us-
851 ing (a) monthly averaging windows (calculated using the cen-
852 tered/running mean and standard deviation); or (b) a window the
853 length of the entire dataset. 46

854	4	Year-by-year time series ridge, zonal, pre-trough, trough, post-	
855		trough, and unclassified patterns based on the monthly-window	
856		anomalies for (a) January and (b) June. The rightmost bar shows	
857		the mean breakdown for all years and are equivalent to the Jan-	
858		uary and June bars in Fig. 3a.	47
859	5	Synoptic properties for the four archetypal synoptic regimes in	
860		June (calculated from the monthly averaging windows using the	
861		centered/running mean and standard deviation), including 500-	
862		mb geopotential heights and anomalies, 1000-mb geopotential	
863		height, 500-mb vertical velocity, and EIS.	48
864	6	Cloud properties for the four archetypal synoptic regimes in	
865		June. For each regime, fields plotted are total ERA-I conden-	
866		sate, total cloud fraction, and cloud-top temperature, and total	
867		cloud fraction and cloud-top temperature from MODIS. Vertical	
868		bars show the the frequency of occurrence of cloud fractions of	
869		0.1 and 0.9 at the ERA-I grid point nearest to the Azores.	49
870	7	As in Fig. 5 but for January. The 5×5 node map for January	
871		from which these specific nodes are drawn (corresponding to	
872		Fig. 2 for the June nodes) is shown in Fig. S1.	50
873	8	As in Fig. 6 but for January.	51

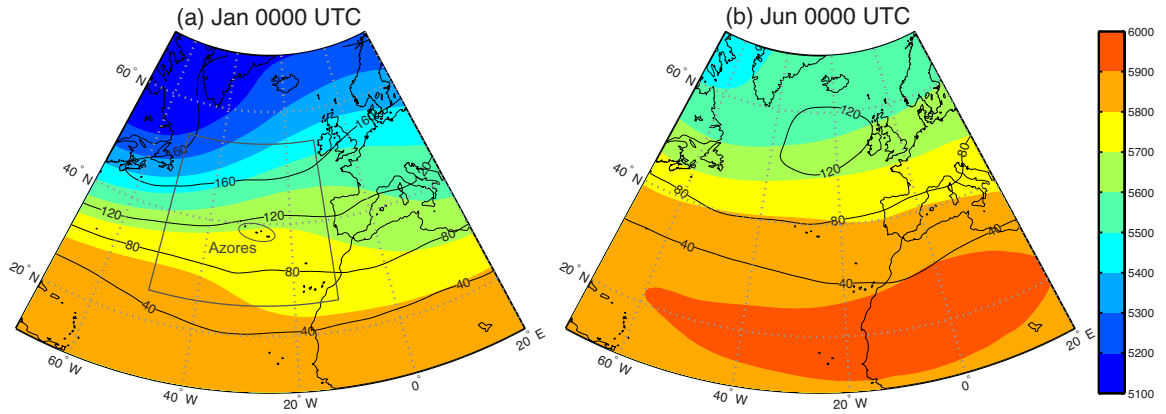


Fig. 1. Mean 500-mb heights for January and June. The inner box in the top map represents the smaller domain used to explore variability in the vicinity of the Azores. Black contour lines are standard deviation of the mean 500-mb height, and can be used as a proxy for storm track variability, where higher numbers indicate higher variability.

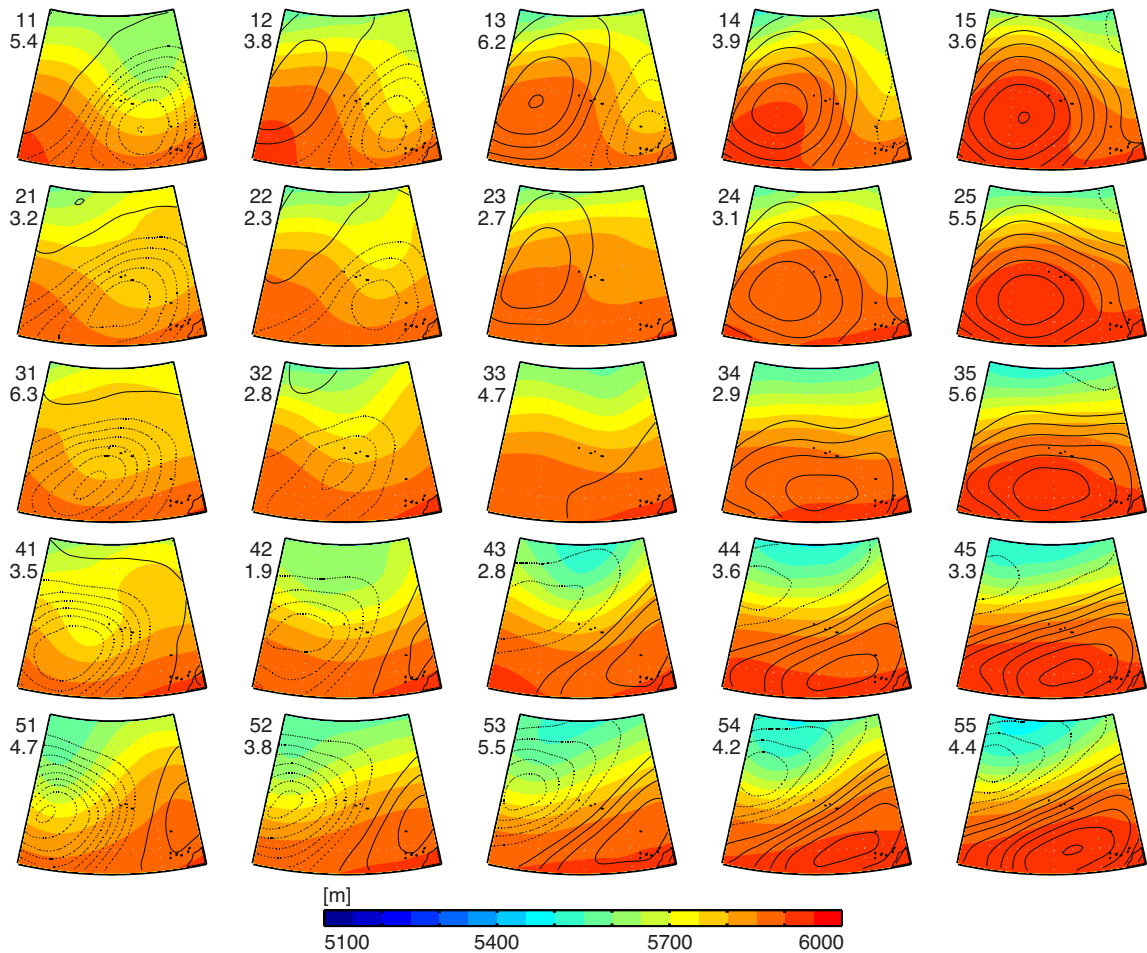


Fig. 2. Monthly-window SOM nodes of 500-mb geopotential heights with overlaid contours of normalized 500-mb geopotential height anomalies (using mean and standard deviation values calculated over a 31-day window centered on each day) for June. The contour interval for the height anomalies is 0.1 [nondimensional]. The numbers in the upper left-hand portion of each node indicate node number in matrix notation, and the relative frequency of occurrence of each node.

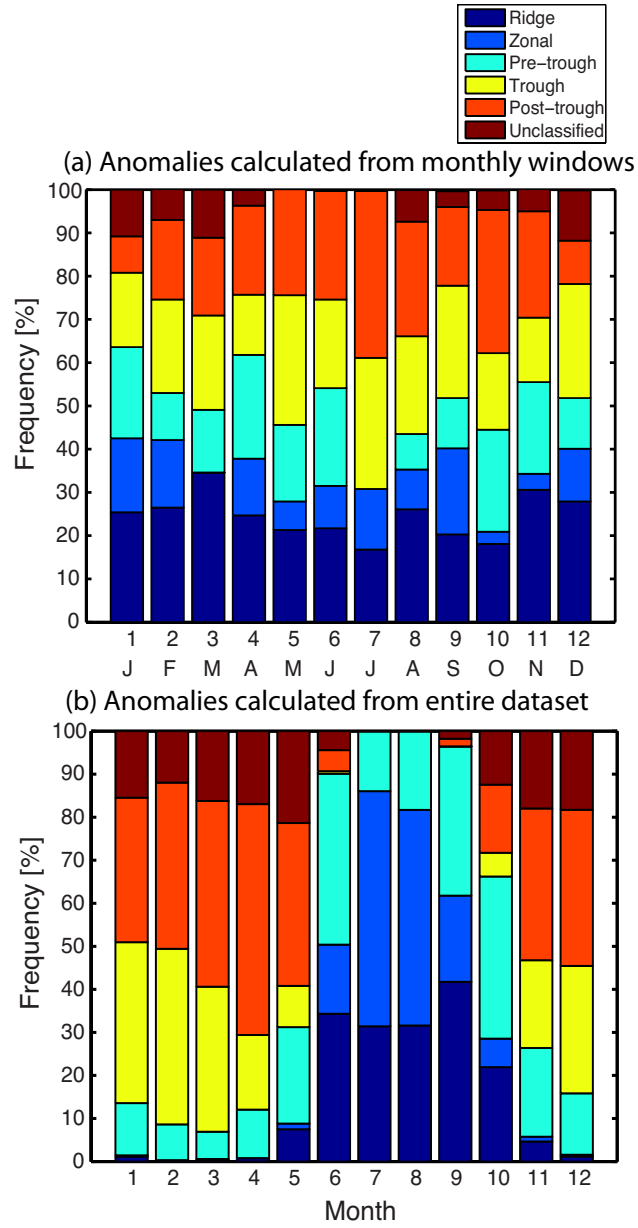


Fig. 3. Annual cycle of ridge, zonal, pre-trough, trough, post-trough, and unclassified patterns based on the anomalies calculated using (a) monthly averaging windows (calculated using the centered/running mean and standard deviation); or (b) a window the length of the entire dataset.

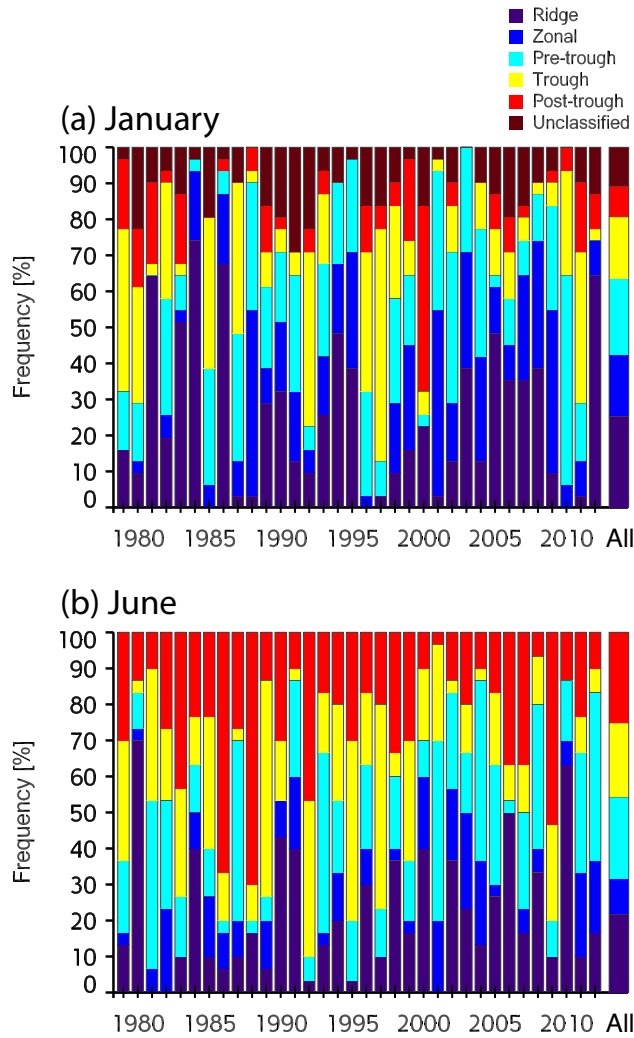


Fig. 4. Year-by-year time series ridge, zonal, pre-trough, trough, post-trough, and unclassified patterns based on the monthly-window anomalies for (a) January and (b) June. The rightmost bar shows the mean breakdown for all years and are equivalent to the January and June bars in Fig. 3a.

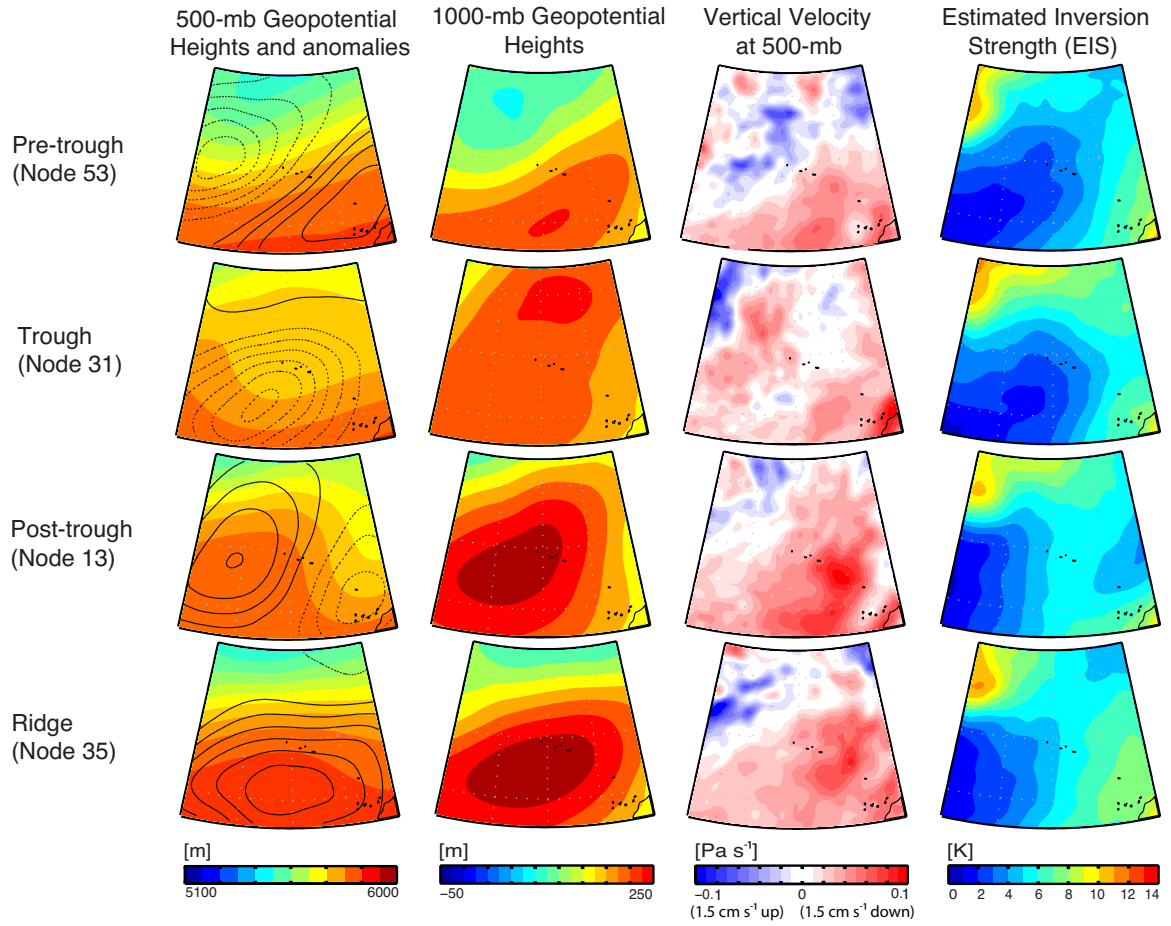


Fig. 5. Synoptic properties for the four archetypal synoptic regimes in June (calculated from the monthly averaging windows using the centered/running mean and standard deviation), including 500-mb geopotential heights and anomalies, 1000-mb geopotential height, 500-mb vertical velocity, and EIS.

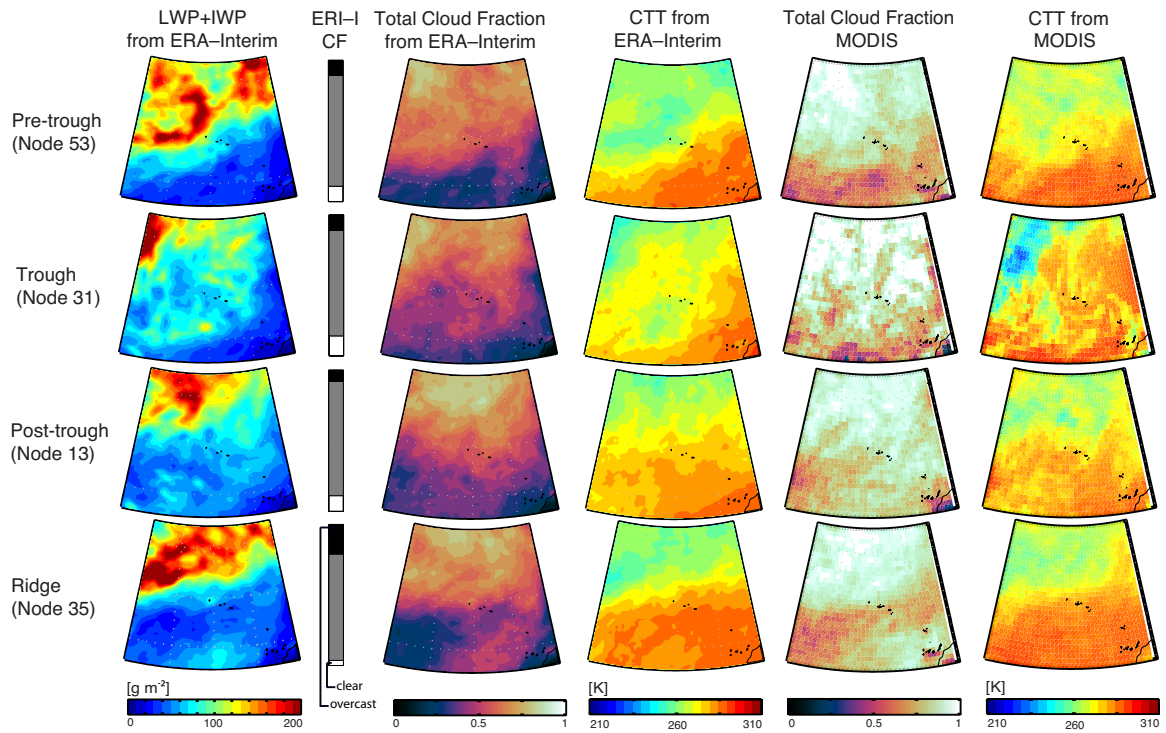


Fig. 6. Cloud properties for the four archetypal synoptic regimes in June. For each regime, fields plotted are total ERA-I condensate, total cloud fraction, and cloud-top temperature, and total cloud fraction and cloud-top temperature from MODIS. Vertical bars show the the frequency of occurrence of cloud fractions of 0.1 and 0.9 at the ERA-I grid point nearest to the Azores.

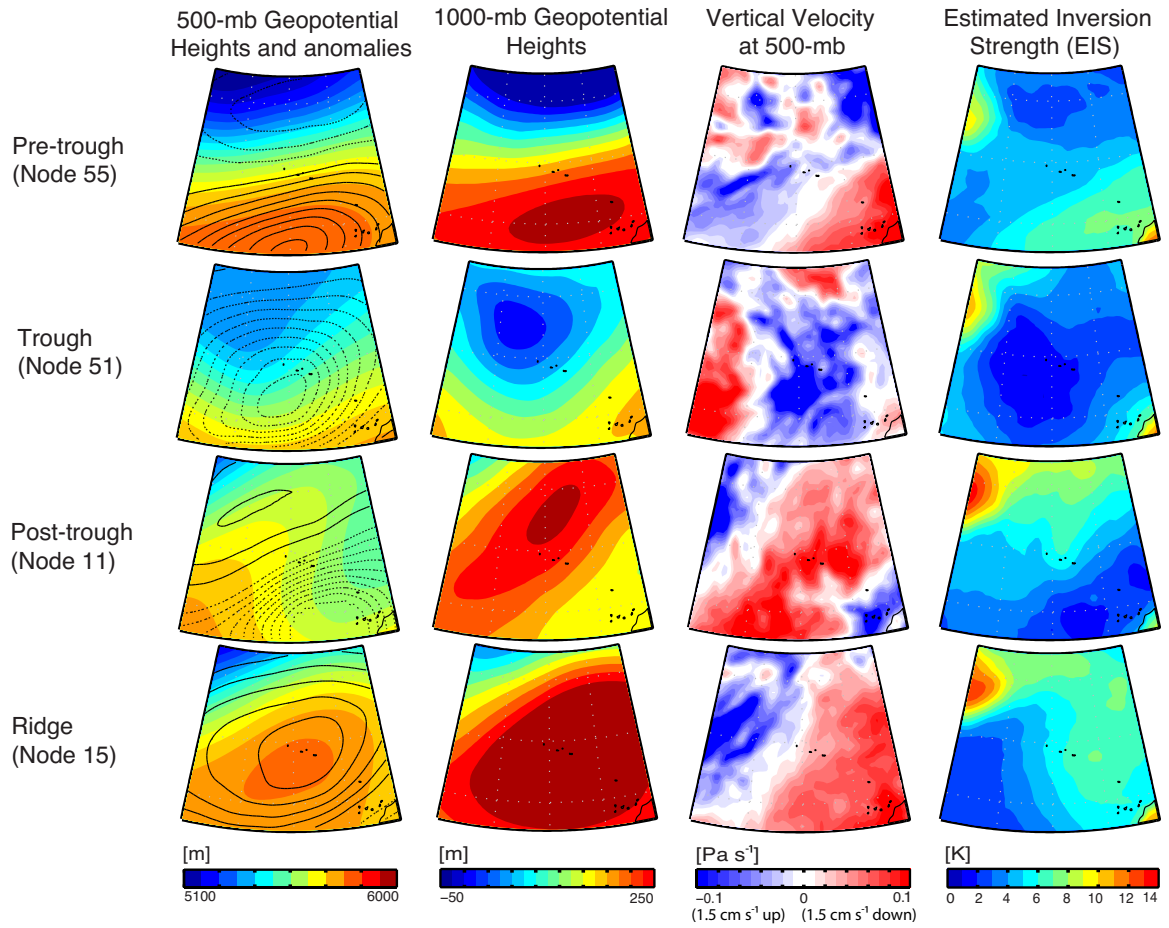


Fig. 7. As in Fig. 5 but for January. The 5×5 node map for January from which these specific nodes are drawn (corresponding to Fig. 2 for the June nodes) is shown in Fig. S1.

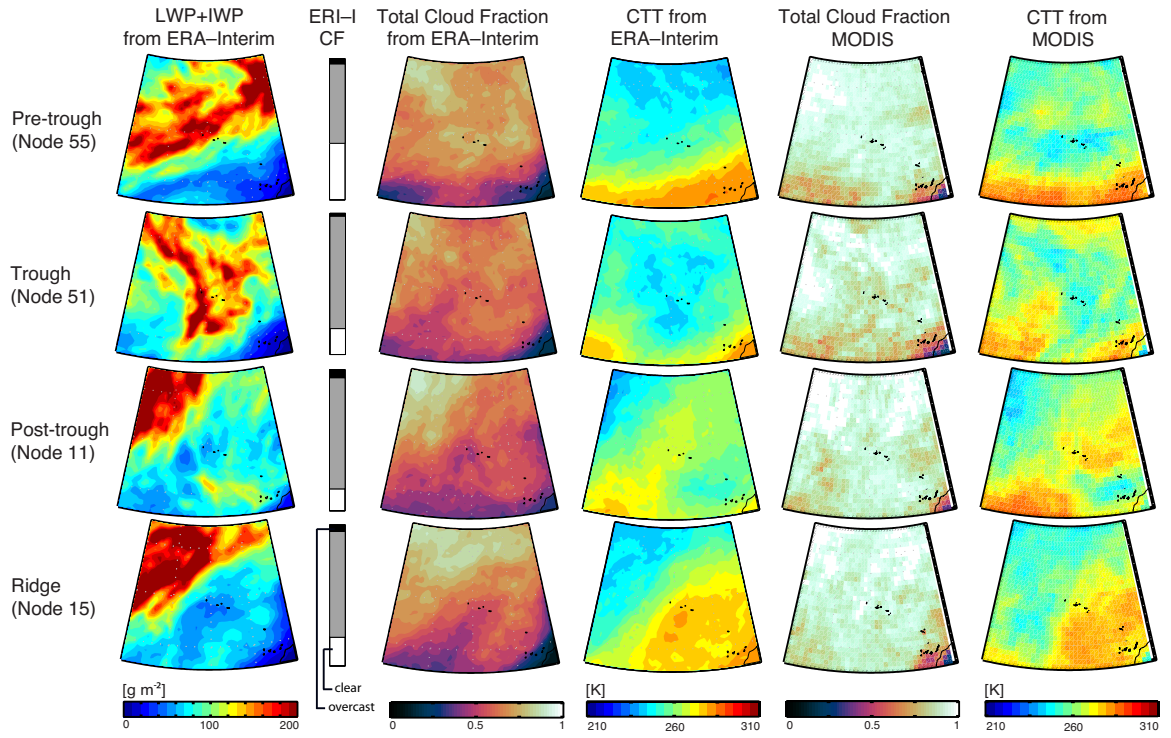


Fig. 8. As in Fig. 6 but for January.

Table 1: Percentages of synoptic patterns experienced during each month calculated using classifications based on anomalies calculated from monthly averaging windows.

	Pre-trough	Trough	Post-trough	Ridge	Zonal	Unclassified
JAN	21.1	17.2	8.4	25.4	17.1	10.8
FEB	10.9	21.6	18.4	26.5	15.6	7.1
MAR	14.5	21.8	18.0	34.6	0.0	11.1
APR	24.0	13.9	20.6	24.7	13.1	3.6
MAY	17.7	30.0	24.5	21.3	6.6	0.0
JUN	22.6	20.5	25.1	21.7	9.8	0.0
JUL	0.0	30.3	38.6	16.8	14	0.0
AUG	8.2	22.6	26.5	26.1	9.2	7.3
SEP	11.6	26.0	18.2	20.3	19.9	3.6
OCT	23.6	17.7	33.1	18.1	2.8	4.5
NOV	21.2	14.9	24.6	30.6	3.7	5.1
DEC	11.7	26.4	10.0	27.9	12.2	11.6

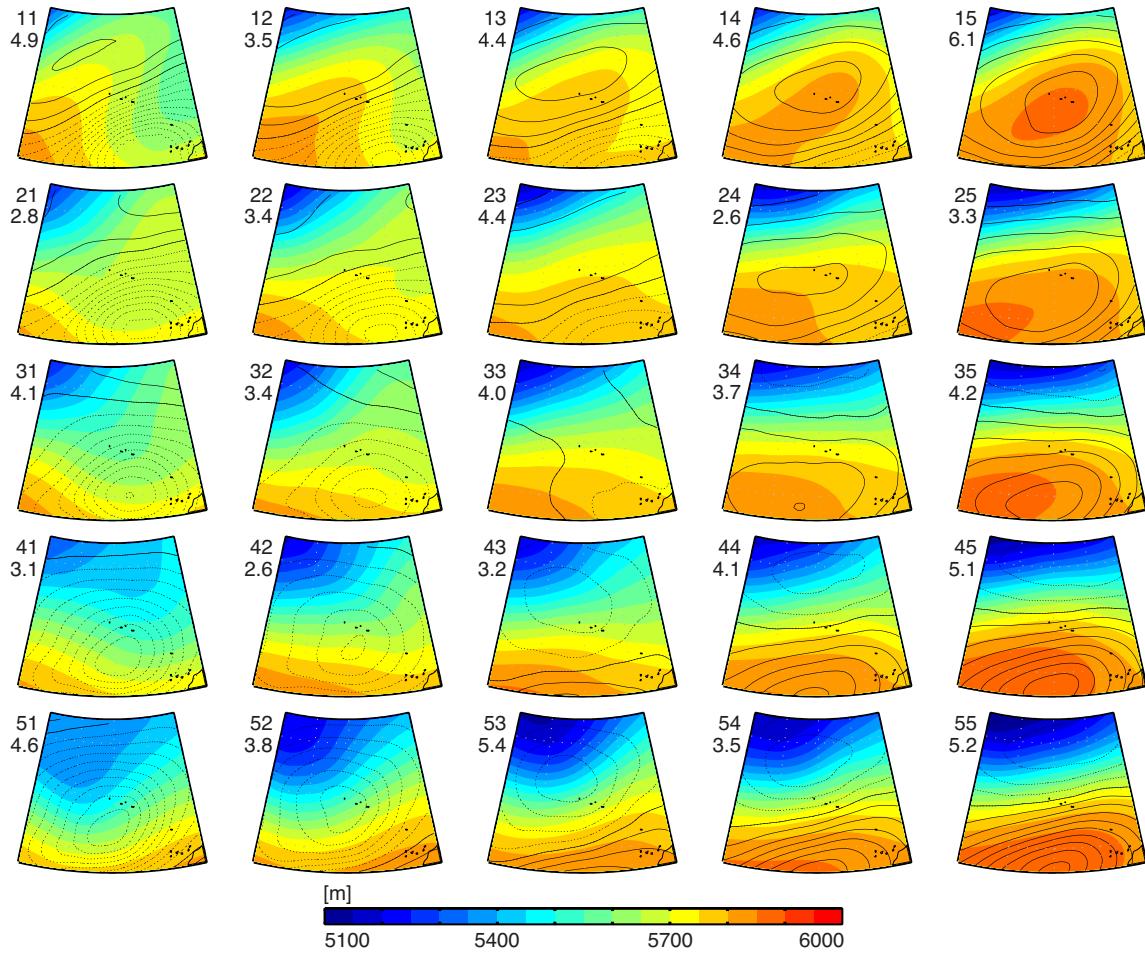
Table 2: Percentages of synoptic patterns experienced during each month calculated using classifications based on anomalies calculated from mean and standard deviation from the entire data record.

	Pre-trough	Trough	Post-trough	Ridge	Zonal	Unclassified
JAN	12.1	37.4	33.6	1.1	0.3	15.5
FEB	8.3	40.8	38.6	0.3	0.0	12.0
MAR	6.4	33.7	43.2	0.4	0.2	16.2
APR	11.3	17.4	53.6	0.8	0.0	17.0
MAY	22.4	9.6	37.9	7.5	1.3	21.3
JUN	39.7	0.6	4.9	34.3	16.1	4.4
JUL	13.9	0.0	0.0	31.4	54.6	0.0
AUG	18.3	0.0	0.0	31.6	50.1	0.0
SEP	34.7	0.0	1.8	41.8	20.0	1.8
OCT	37.7	5.5	15.8	21.9	6.6	12.4
NOV	20.6	20.4	35.3	4.6	1.1	18.0
DEC	14.3	29.6	36.3	1.2	0.4	18.3

Supplemental figures

The supplemental figures S1–S12 represent the SOM nodes of 500-mb geopotential height with overlaid contours of normalized 500-mb geopotential height anomalies for the given month. These nodes are calculated from the anomalies obtained from mean and standard deviation values taken over 31-day centered windows. The SOM node map in Figure S6 is equivalent to that in Fig. 2 in the manuscript but is included for completeness. The supplemental figures also include the classification of each node into different synoptic categories, as described in the text.

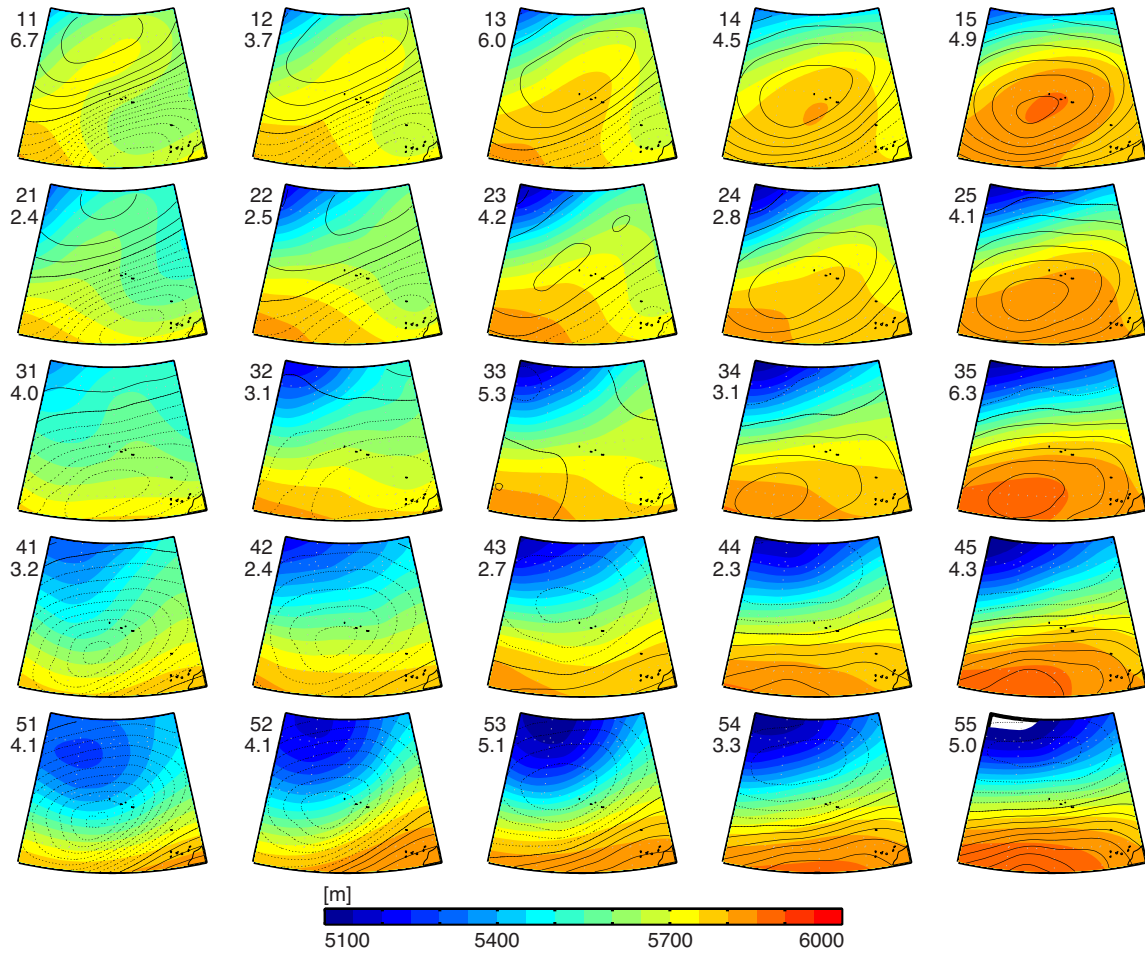
JAN



Pre-trough: 43, 52, 53, 54, 55
 Trough: 21, 31, 41, 42, 51
 Post-trough: 11, 12
 Ridge: 13, 14, 15, 23, 24, 25
 Zonal: 34, 35, 44, 45
 Unclassified: 22, 32, 33

Figure S1: SOM nodes of 500-mb geopotential heights with overlaid contours of normalized 500-mb geopotential height anomalies for January. These monthly-window nodes are calculated from the anomalies obtained from mean and standard deviation values taken over 31-day centered windows. The numbers in the upper left-hand portion of each node indicate node number in matrix notation, and the relative frequency of occurrence of each node. Each of the 25 nodes is classified into different synoptic categories, as described in the manuscript.

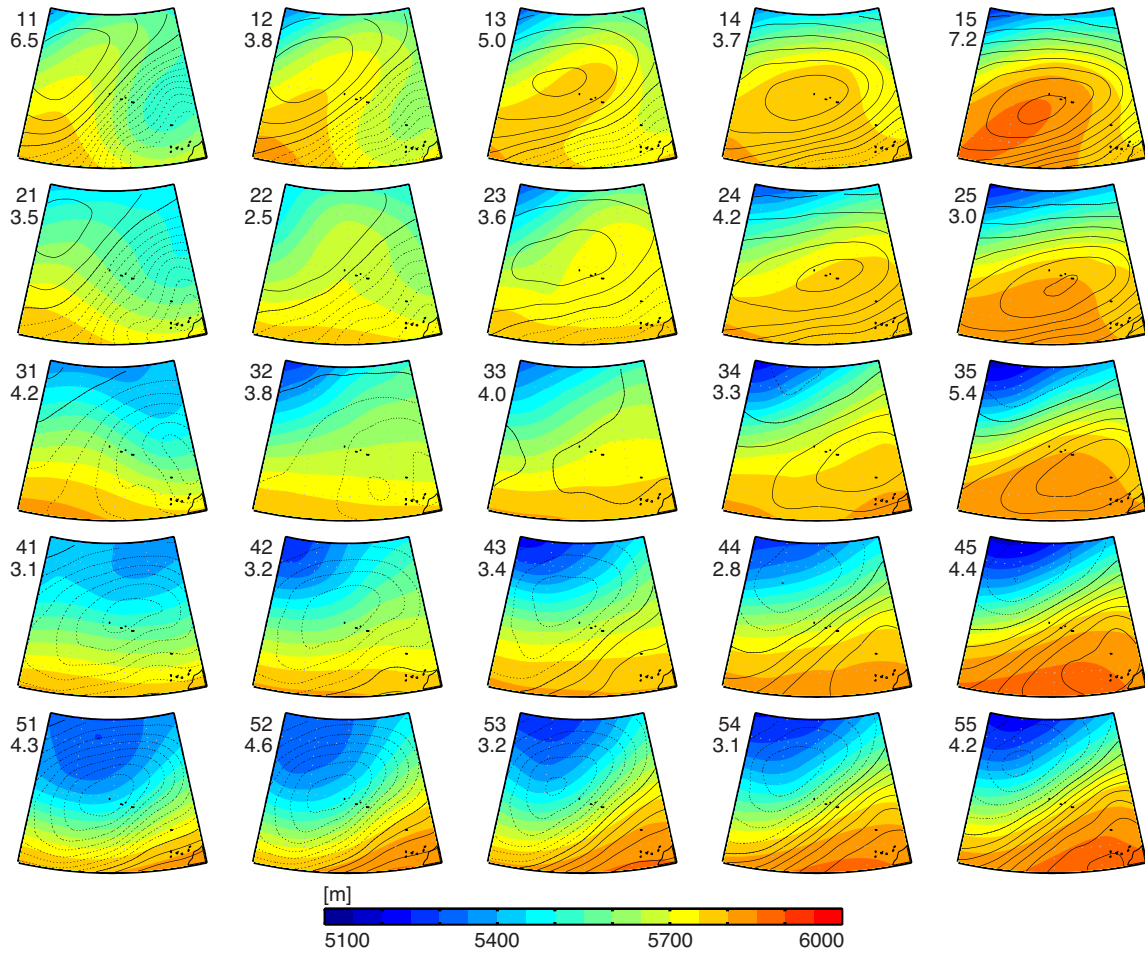
FEB



Pre-trough: 33, 44, 54
Trough: 41, 42, 43, 51, 52, 53
Post-trough: 11, 12, 21, 22, 32
Ridge: 13, 14, 15, 23, 24, 25
Zonal: 35, 45, 55
Unclassified: 31, 34

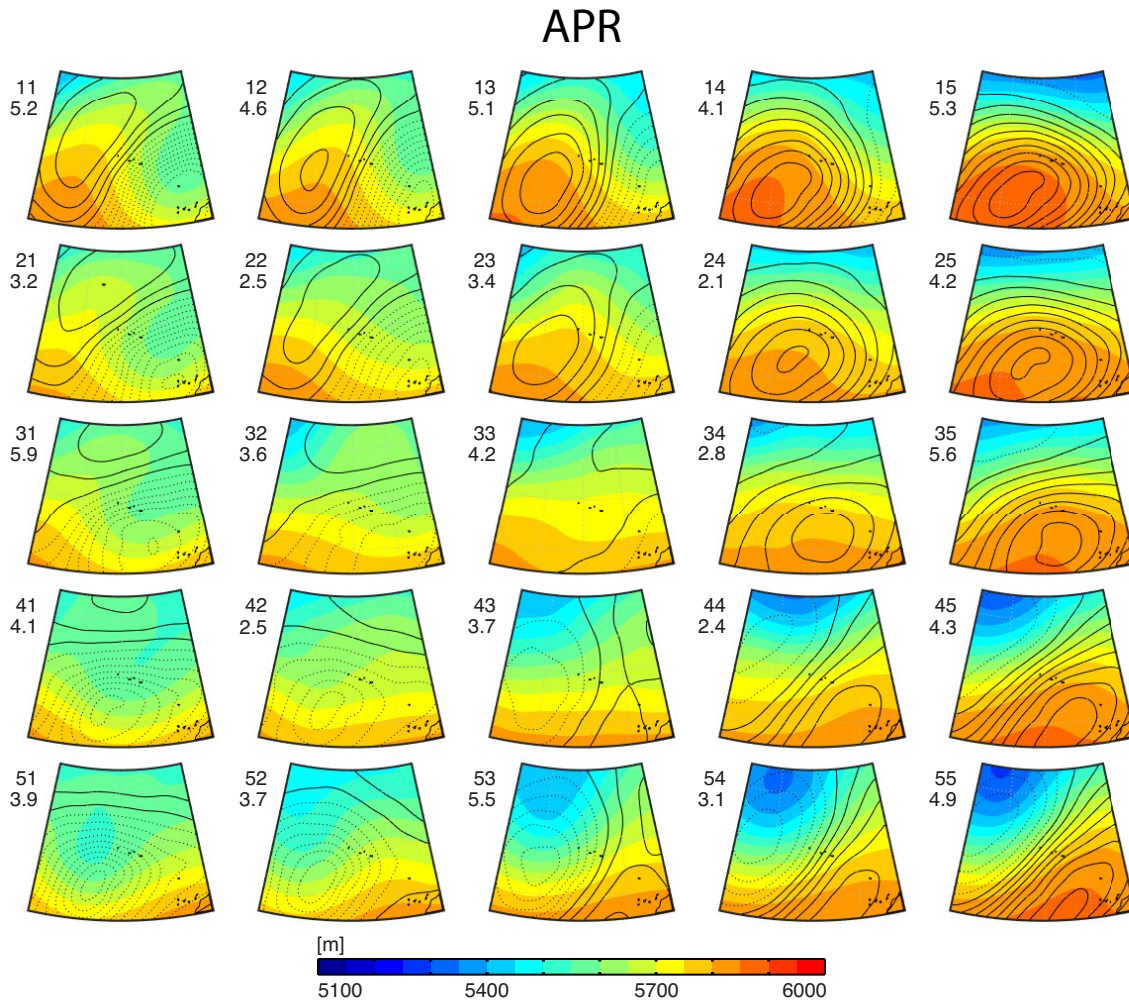
Figure S2: As in Fig. S1 but for February.

MAR



Pre-trough: 44, 45, 54, 55
Trough: 41, 42, 43, 51, 52, 53
Post-trough: 11, 12, 21, 31
Ridge: 13, 14, 15, 22, 23, 24, 25, 35
Zonal: —
Unclassified: 32, 33, 34

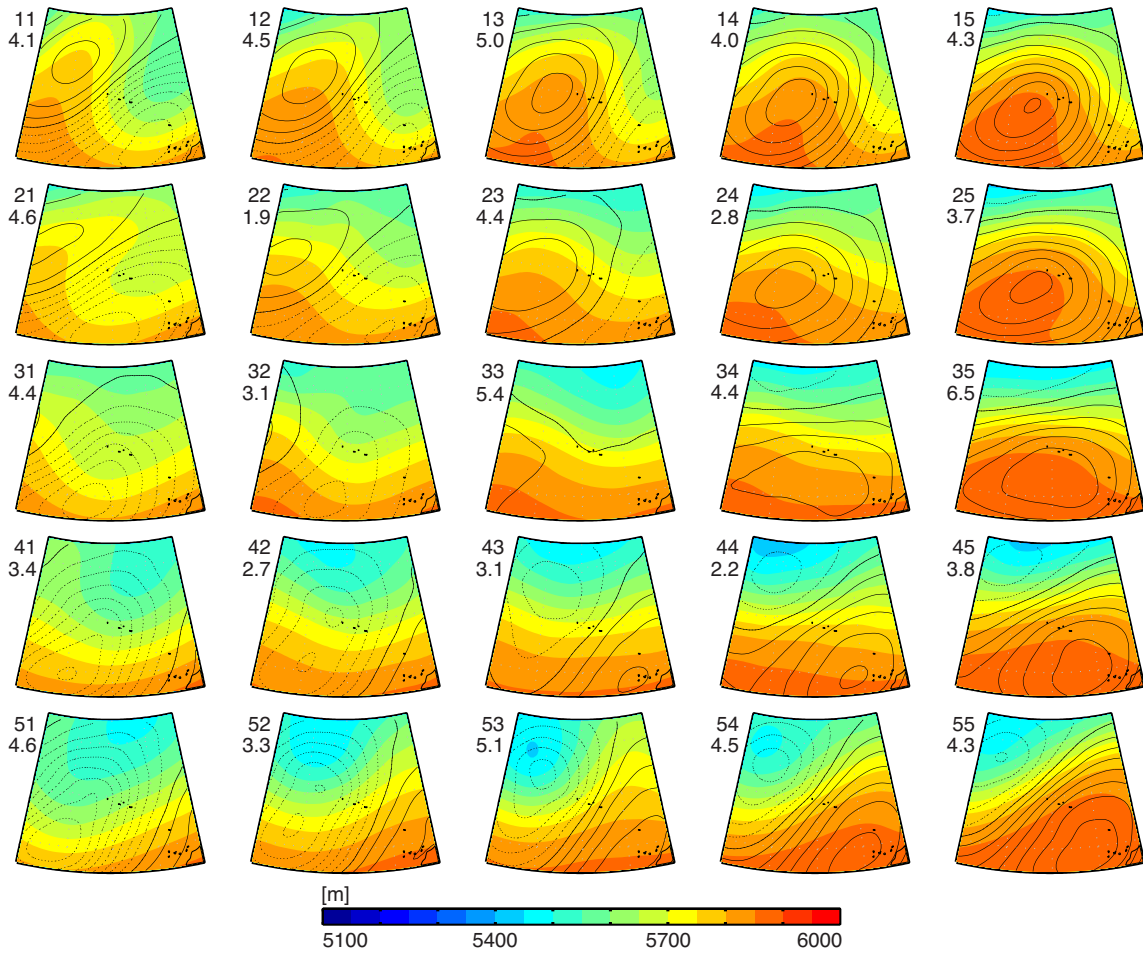
Figure S3: As in Fig. S1 but for March.



Pre-trough: 42, 45, 52, 53, 54, 55
 Trough: 31, 41, 51
 Post-trough: 11, 12, 13, 21, 22
 Ridge: 14, 15, 23, 24, 25, 35
 Zonal: 33, 34, 43, 44
 Unclassified: 32

Figure S4: As in Fig. S1 but for April.

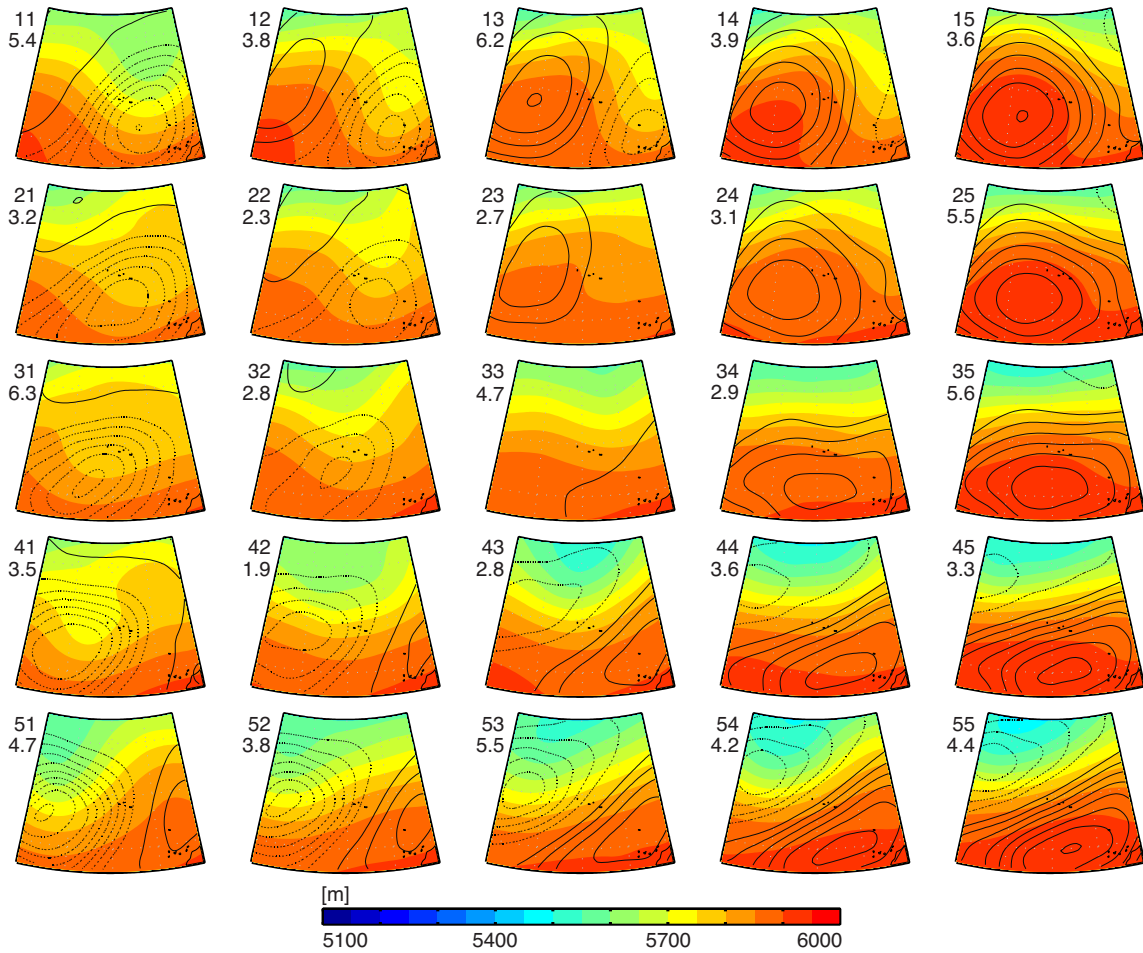
MAY



- Pre-trough: 45, 53, 54, 55
- Trough: 31, 32, 33, 41, 42, 43, 51, 52
- Post-trough: 11, 12, 13, 21, 22, 23
- Ridge: 14, 15, 24, 25, 35
- Zonal: 34, 44
- Unclassified: —

Figure S5: As in Fig. S1 but for May.

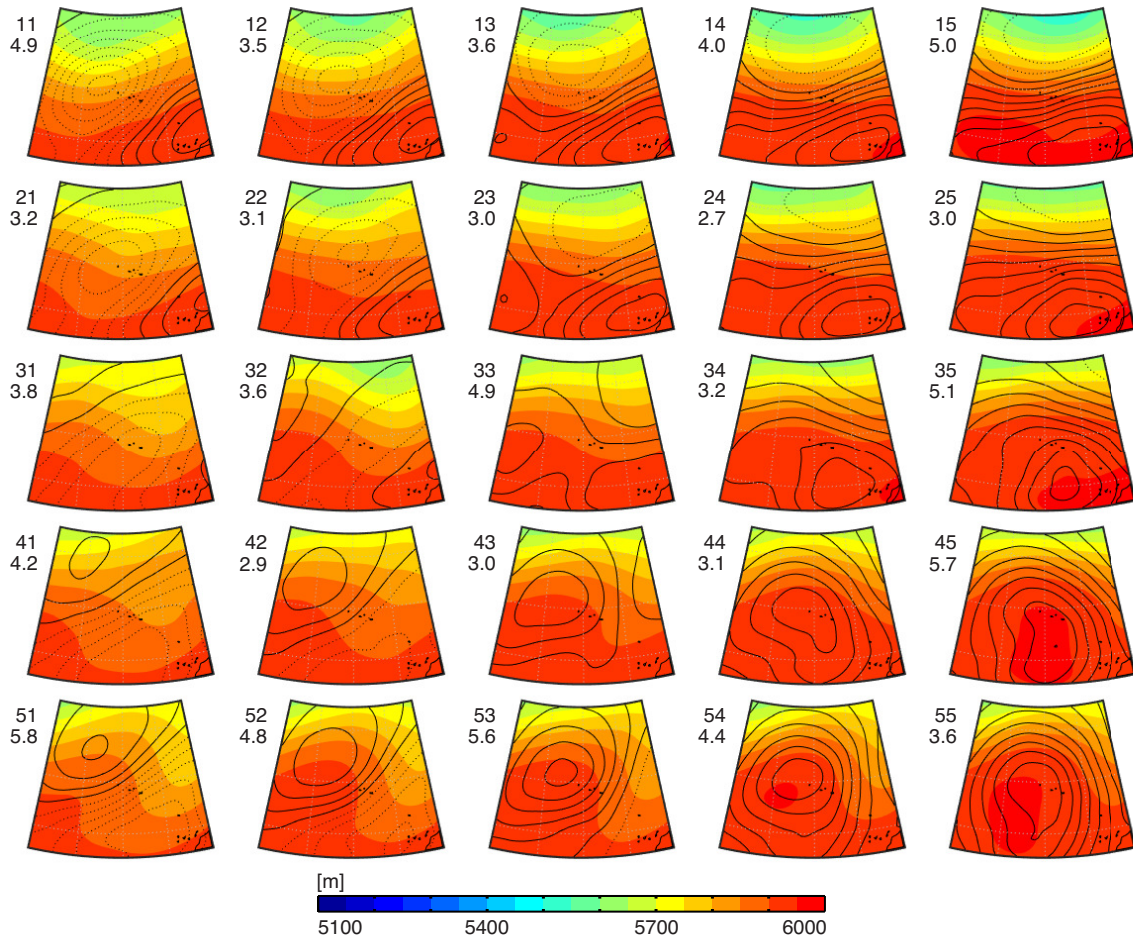
JUN



Pre-trough: 51, 52, 53, 54, 55
Trough: 21, 31, 32, 41, 42, 43
Post-trough: 11, 12, 13, 22, 23, 33
Ridge: 14, 15, 24, 25, 35
Zonal: 34, 44
Unclassified: —

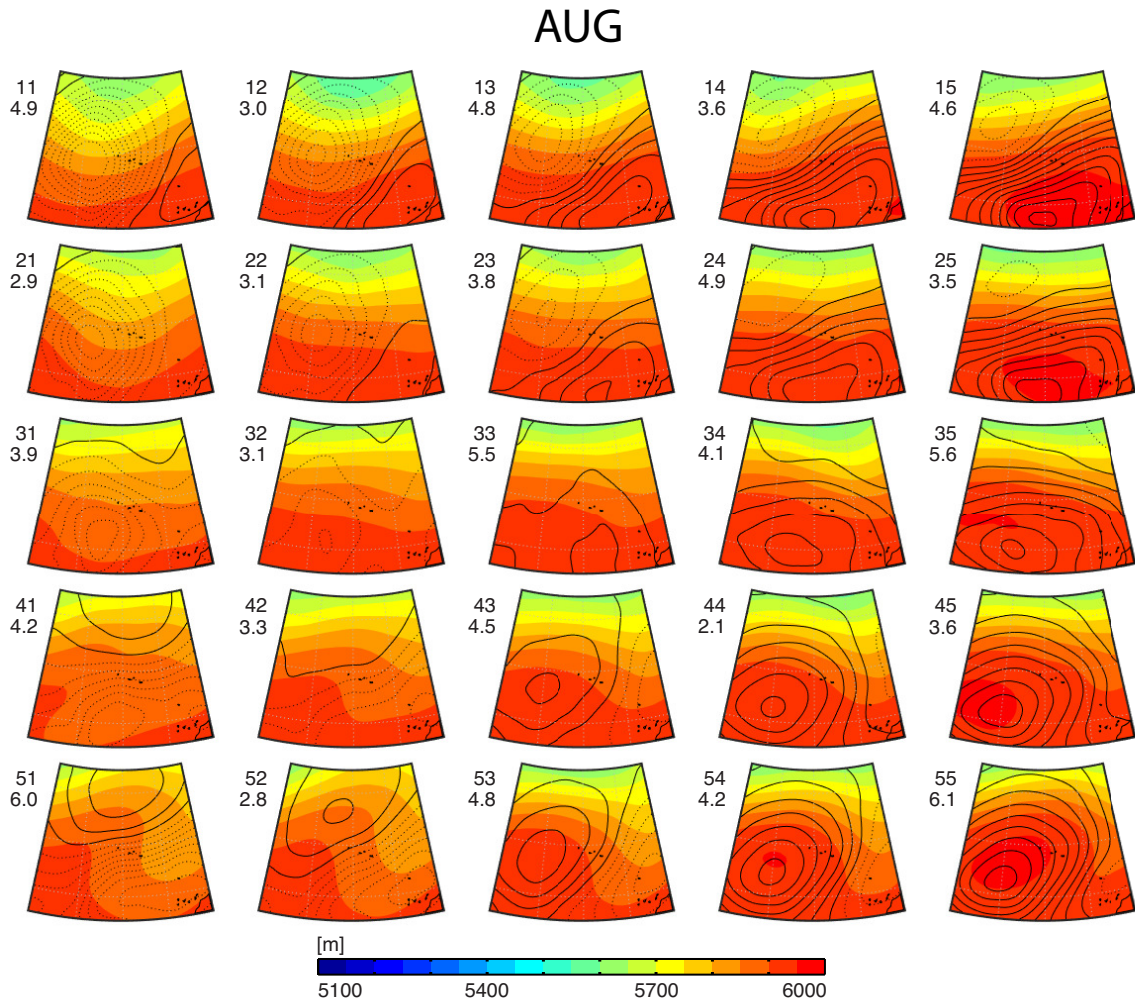
Figure S6: As in Fig. S1 but for June.

JUL



Pre-trough: —
Trough: 11, 12, 13, 14, 15, 21, 22, 23
Post-trough: 31, 32, 33, 41, 42, 43, 51, 52, 53
Ridge: 44, 45, 54, 55
Zonal: 24, 25, 34, 35
Unclassified: —

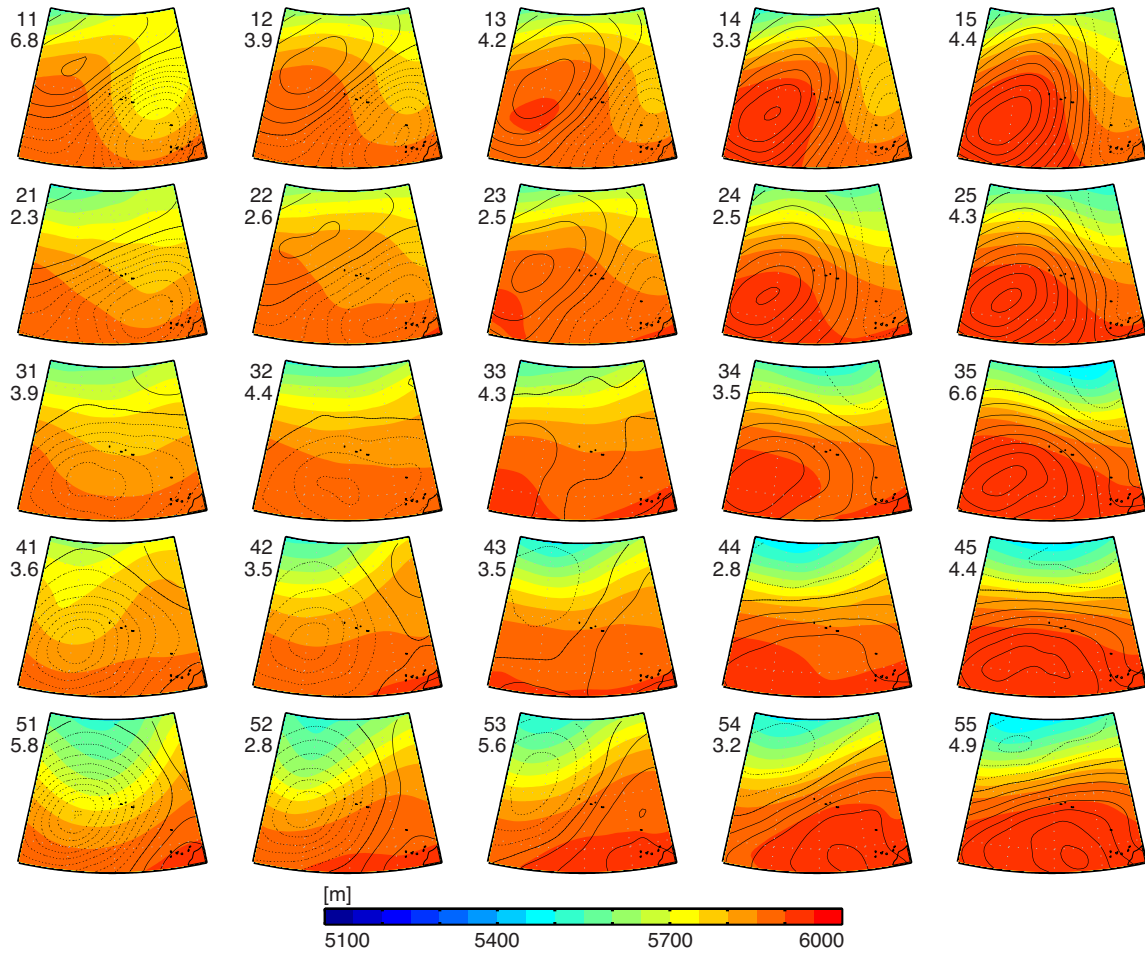
Figure S7: As in Fig. S1 but for July.



Pre-trough: 14, 15
 Trough: 11, 12, 13, 21, 22, 31
 Post-trough: 33, 34, 42, 51, 52, 53
 Ridge: 35, 43, 44, 45, 54, 55
 Zonal: 23, 24, 25
 Unclassified: 32, 41

Figure S8: As in Fig. S1 but for August.

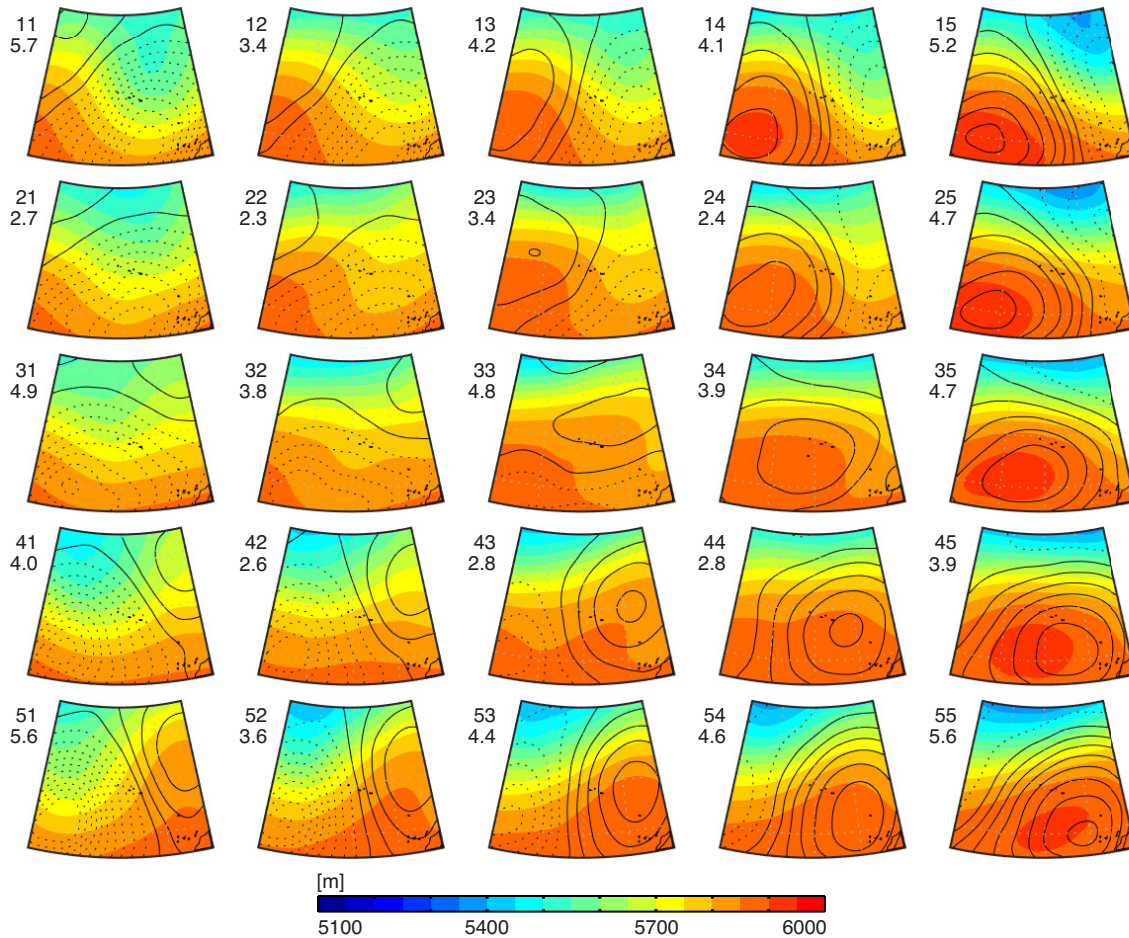
SEP



Pre-trough: 52, 53, 54
Trough: 21, 22, 31, 32, 42, 43, 51
Post-trough: 11, 12, 13, 14
Ridge: 15, 23, 24, 25, 35
Zonal: 33, 34, 44, 45, 55
Unclassified: 41

Figure S9: As in Fig. S1 but for September.

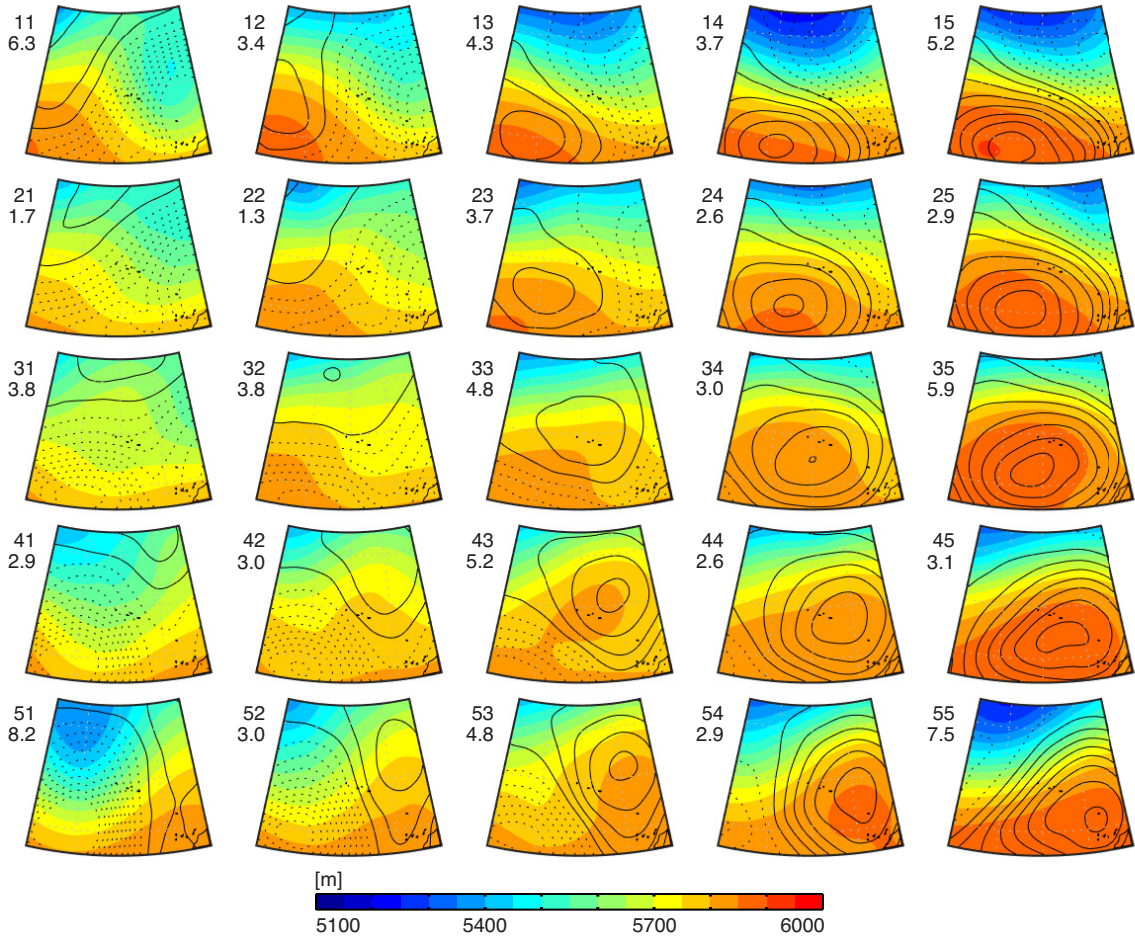
OCT



Pre-trough: 42, 43, 51, 52, 53, 54
Trough: 21, 22, 31, 32, 41
Post-trough: 11, 12, 13, 14, 15, 23, 24, 25
Ridge: 34, 35, 45, 55
Zonal: 44
Unclassified: 33

Figure S10: As in Fig. S1 but for October.

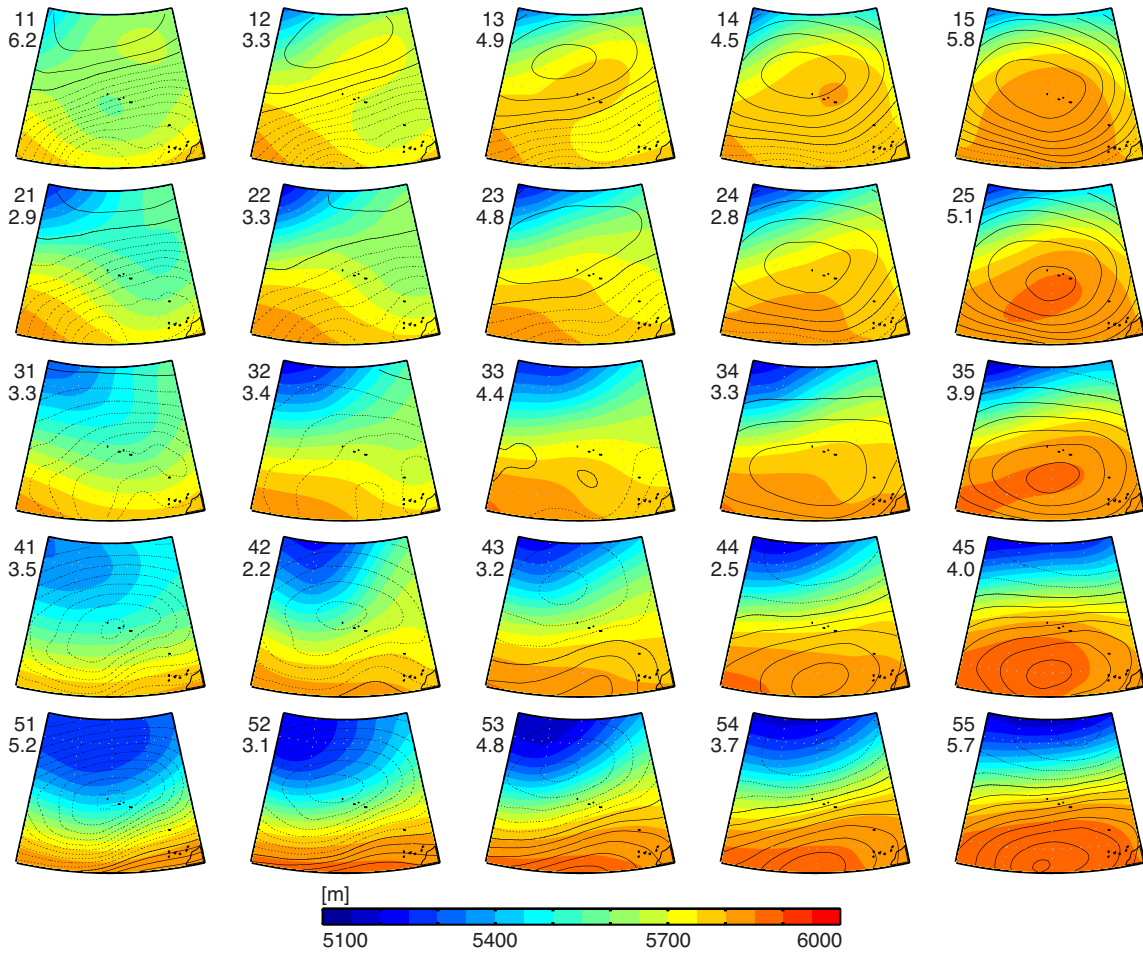
NOV



Pre-trough: 42, 44, 52, 53, 54, 55
Trough: 31, 41, 51
Post-trough: 11, 12, 13, 14, 15, 21
Ridge: 24, 25, 33, 34, 35, 43, 45
Zonal: 23
Unclassified: 22, 32

Figure S11: As in Fig. S1 but for November.

DEC



- Pre-trough: 43, 53, 54
- Trough: 11, 21, 31, 41, 42, 51, 52
- Post-trough: 12, 22, 32
- Ridge: 13, 14, 15, 23, 24, 25
- Zonal: 44, 45, 55
- Unclassified: 33, 34, 35

Figure S12: As in Fig. S1 but for December.